Geophysical Journal International

Geophys. J. Int. (2022) **228,** 1392–1409 https://doi.org/10.1093/gji/ggab406
Advance Access publication 2021 October 06
GJI Seismology

Assessment of seismic tomographic models of the contiguous United States using intermediate-period 3-D wavefield simulation

Tong Zhou[1,*] Ziyi Xi,[1] Min Chen[1,2] and Jiaqi Li[1]

[1] *Department of Computational Mathematics, Science and Engineering, Michigan State University, East Lansing, Michigan 48824, USA. E-mail: tzhou@epss.ucla.edu*
[2] *Department of Earth and Environmental Sciences, Michigan State University, East Lansing, Michigan 48824, USA*

Accepted 2021 October 4. Received 2021 September 16; in original form 2021 May 26

SUMMARY

The contiguous United States has been well instrumented with broad-band seismic stations due to the development of the EarthScope Transportable Array. Previous studies have provided various 3-D seismic wave speed models for the crust and upper mantle with improved resolution. However, discrepancies exist among these models due to differences in both data sets and tomographic methods, which introduce uncertainties on the imaged lithospheric structure beneath North America. A further model refinement using the best data coverage and advanced tomographic methods such as full-waveform inversion (FWI) is expected to provide better seismological constraints. Initial models have significant impacts on the convergence of FWIs. However, how to select an optimal initial model is not well investigated. Here, we present a data-driven initial model selection procedure for the contiguous US and surrounding regions by assessing waveform fitting and misfit functions between the observations and synthetics from candidate models. We use a data set of waveforms from 30 earthquakes recorded by 5820 stations across North America. The results suggest that the tested 3-D models capture well long-period waveforms while showing discrepancies in short periods especially on tangential components. This observation indicates that the smaller scale heterogeneities and radial anisotropy in the crust and upper mantle are not well constrained. Based on our test results, a hybrid initial model combining S40RTS or S362ANI in the mantle and US.2016 for V_{sv} and CRUST1.0 for V_{sh} in the crust is compatible for future FWIs to refine the lithospheric structure of North America.

Key words: North America; Waveform inversion; Computational seismology; Seismic tomography.

1 INTRODUCTION

Seismic tomography provides one of the most important physical constraints of the Earth's interior structure and offers insight into the dynamic processes of the lithosphere and asthenosphere. Tomographic images of the Earth's interior, facilitated by large-aperture uniform array deployments (e.g. USArray in North America and CEArray in East Asia) have been significantly improved in resolution of the crust and upper-mantle structure (Schmandt & Lin 2014; Yuan *et al.* 2014; Chen *et al.* 2015b; Shen & Ritzwoller 2016; Zhu *et al.* 2017; Krischer *et al.* 2018; Tao *et al.* 2018). Meanwhile, advanced tomographic methods utilizing either multiple data sets (e.g. Shen & Ritzwoller 2016) or advanced inversion methods such as full-waveform inversion (FWI, e.g. Fichtner *et al.* 2009, 2010; Tape *et al.* 2010; Lekić & Romanowicz 2011; Yuan *et al.* 2014; Chen *et al.* 2015a, 2017; Zhu *et al.* 2017; Krischer *et al.* 2018; Tao *et al.* 2018; Chen *et al.* 2019) have helped remarkably in accurately rendering the physical properties of the crust and upper mantle. Although large-scale structures (on the order of 1000 km) in tomographic models are consistent in general, small-scale structures (on the order of 10–100 km) are still very different in terms of both the amplitude and the pattern of seismic wave speed anomalies. These models also have different geometric mesh and inversion parameters, which brings extra complexity for interpretation.

From the inversion aspect, each model has achieved the minimum misfit for both of its data set and its forward modelling approximation. However, if examining the waveform fitting with a uniform validation data set, discrepancies of model predictions still appear as reported by previous research (Lin *et al.* 2011; Lee *et al.* 2014; Gao & Shen 2015; Bao & Shen 2016; Taborda *et al.* 2016). These

---

[*] Now at: Earth Planetary and Space Sciences, University of California, Los Angeles, CA 90095, USA

discrepancies become more severe when realistic Earth's properties are taken into account, for example, the topography, attenuation and the Earth's ellipticity. Therefore, it is important to further refine the seismic wave speed model of the contiguous US and surrounding regions within an FWI configuration that takes more realistic Earth's properties and larger waveform data sets into consideration.

FWI methods usually minimize the data-synthetics misfit iteratively with gradient-based methods (Tromp *et al.* 2005), which is highly nonlinear and depends on the initial model. A good initial model is reported to be helpful for preventing the inversion from being trapped into a local minimum (Mulder & Plessix 2008; Fichtner *et al.* 2009; Bozdağ *et al.* 2016; Zhu *et al.* 2017; Krischer *et al.* 2018; Zhou *et al.* 2019). Previous FWI studies usually have their own preference in selecting initial models, for example, a 1-D mantle model with 3-D crust (Lekić & Romanowicz 2011), a global 3-D mantle model with CRUST2.0 (Chen *et al.* 2015a; Bozdağ *et al.* 2016; Zhu *et al.* 2017), a hybrid model combining 3-D regional mantle and crustal models (Krischer *et al.* 2018), or a combination of previous FWI models (Yuan *et al.* 2014; Tao *et al.* 2017). Although recent FWI studies mainly focus on the upper-mantle structures, a good crustal model is also significant to FWI (Bozdağ & Trampert 2008; Ritsema *et al.* 2009; Ferreira *et al.* 2010). The initial model selection generally requires better data fitting to satisfy the linear approximation and less artefacts to influence the further iterations. However, this issue is not systematically and quantitatively discussed.

It is effective to compare tomographic models by assessing the misfit of the observation and the model predictions by numerical simulations (Alex Song & Helmberger 2007; Qin *et al.* 2009; Bozdağ & Trampert 2010; Gao & Shen 2012; Lee *et al.* 2014; Gao & Shen 2015; Maceira *et al.* 2015; Bao & Shen 2016; Taborda *et al.* 2016). These comparisons suggest that ray theory based traveltime tomographic models generally recover the patterns of wave speed variations but not the full wave speed contrast, thus are unable to reproduce accurate waveform distortions (Alex Song & Helmberger 2007). Tomographic models utilizing more data coverage and/or FWI methods tend to have better predictability of the waveforms (Gao & Shen 2012, 2015). However, the predictability of tomographic models with a 3-D waveform simulation method considering realistic attenuation, topography, gravity and ellipticity is still unknown. Such predictability not only tells the compatibility of these models to a realistic configuration of 3-D numerical waveform simulation, but also serves as an indication for selecting initial model for FWI with realistic properties taken into consideration.

The contiguous US has been well instrumented and extensively investigated by many tomographic studies (Engdahl *et al.* 1998; Bedle & van der Lee 2009; Schmandt & Humphreys 2010; Lin *et al.* 2012; Pavlis *et al.* 2012; Lin *et al.* 2014; Porritt *et al.* 2014; Schmandt & Lin 2014; Yuan *et al.* 2014; Schmandt *et al.* 2015; Shen & Ritzwoller 2016; Buehler & Shearer 2017; Burdick *et al.* 2017; Zhu *et al.* 2017; Jiang *et al.* 2018; Krischer *et al.* 2018; Nelson & Grand 2018) with different data sets and tomographic methods. This provides us a good example of assessing different regional and global seismic models and discuss how to construct a compatible and optimal initial model for FWI with a mesh considering more realistic Earth's properties.

In this work, we aim at building an initial model for FWI with realistic configurations by comparing the waveform predictability of several recent shear wave speed models of the contiguous US and surrounding regions. We define predictability as the waveform fitting between model predictions and observations for each model measured by misfit functions used in FWIs. We systematically analyse each model using a uniform test data set and a spectral-element method (SEM) based wave equation solver SPECFEM3D_GLOBE (Komatitsch & Tromp 2002a, b) with the consideration of topography, attenuation, gravity and Earth's ellipticity. We investigate multiple misfit functions including frequency-dependent traveltime misfit, amplitude misfit, waveform misfit (Tromp *et al.* 2005) and the normalized zero-lag cross-correlation coefficient (NZCC) misfit (Tao *et al.* 2017) of body and surface waves in intermediate-period ranges. Especially, the NZCC is sensitive to both arrival time and waveform similarity between data and synthetics, which is more indicative of the model's predictability for seismic data than the commonly used criterion of traveltime misfit derived from cross correlation.

In the following sections, first, we introduce the seismic models selected for comparison. Then, we systematically compare the waveforms and statistical result of misfit functions for different models in three different intermediate-period ranges, 9–20, 20–40 and 40–120 s. Lastly, we discuss the effectiveness, difficulty and insight of the initial model selection based on model assessment.

2 DATA AND METHODS

2.1 Seismic models for comparison

In this study, we focus on the shear wave speed models since P waves are generally better predicted. We present seven publicly available models which have the resolution for the contiguous US and surrounding regions, including a differential traveltime tomographic model US-SL-2014 (Schmandt & Lin 2014), an ambient noise and receiver function jointly inverted model US.2016 (Shen & Ritzwoller 2016), two FWI models SEMum-NA14 (Yuan *et al.* 2014) and Krischer18 (Krischer *et al.* 2018), and three global tomographic models GyPSuM (Simmons *et al.* 2010) inverted from traveltimes and geodynamic constraints, S362ANI and S40RTS (Kustowski *et al.* 2008; Ritsema *et al.* 2011) both constrained by traveltimes, long-period body waves and surface wave dispersion. The global 1-D model AK135 (Kennett *et al.* 1995) is also selected as a reference to compare with the 3-D models. The method and data set used for each model are briefly summarized in Table 1. We select these models as examples to search for an optimal initial model for future FWI because of two main reasons: (1) these models are generated by various of tomographic methods and seismic data set, which allows the maximum variety of the models. (2) some of the contiguous US models with highest resolution are included.

All 3-D models share similar large-scale pattern of shear wave speed anomalies in the upper mantle (Fig. 1), that is, relatively low wave speeds (low-V) in the western US and relatively high wave speeds (high-V) in the central and eastern US. However, the small-scale anomalies of 10–100 km differ dramatically in terms of not only the anomaly pattern but also the amplitude, which are caused by different data sets and methods used in the tomographic studies. For example, models US-SL-2014, US.2016 and Krischer18 clearly capture the Yellowstone hotspot in the northwestern US, while the other three miss this small-scale feature possibly due to the lack of resolution because of either sparse data coverage or long-wavelength seismic waves used in the inversion. It is notable that the FWI model Krischer18, although derived from long-wavelength seismic waves, can already capture small-scale structures such as the Yellowstone hotspot. This further indicates that the FWI has the advantage of achieving subwavelength resolution (van der Kruk *et al.* 2015). However, in the case of lacking high-frequency data

Table 1. Summary of the seismic models for validation.

Models	Measurement	Data set and frequency range	Model coverage
AK135	TT	Global stations before 1995	Global V_p, V_s, ρ
CRUST1.0	SF, RF, ACT	Global stations before 2013	Global layered crust V_p, V_s, ρ and Moho depth
GyPSuM	TT, GRA, GD	Global stations 1964–2007, 14–100 s	Global V_p, V_s and ρ, 0–2900 km
S40RTS	TT, SF, NM	Global stations before 2011	Global V_p, V_s and ρ
US-SL-2014	TTR	USArray, NCEDC, SCEDC, 2011–2014, 1–20 s	$\delta\ln\mathrm{V_p}$ and $\delta\ln\mathrm{V_s}$, Contiguous US, 60–1220 km
SEMum-NA14	FWI, NM	USArray, North America stations before 2013, 40–120 s	V_{sv} and V_{sh}, 10–80N, 30–330W, 50–410 km
US.2016	ANT, SF, HV, RF	USArray stationss, 2006–2016, 8–90 s	V_s and Moho depth, Contiguous US, 0–150 km
Krischer18	FWI	FDSN hosted stations, 2005–2016, 30–120 s	V_p, V_{sv} and V_{sh}, 0–1440 km, North America and North Atlantic
S362ANI	TT, SF, WF	Global stations from 1994–2003, 50–200 s for WF and 35–150 s for SF	V_{sv} and V_{sh}, 25–2890 km, Global

Notes: Abbreviations for types of measurements: ACT: active source survey; ANT: ambient noise; FWI: full waveform inversion; GD: geodetic measurements; GRA: gravity measurements; HV: H/V ratio (Rayleigh wave ellipticity); NM: normal mode; RF: receiver function; SF: surface wave dispersion; TT: traveltime; TTR: traveltime residuals; WF: waveform inversion using path average approximation.

Abbreviations for model velocities: V_s: shear wave speed; V_p: *P*-wave speed; V_{sh} horizontally travelling and horizontally polarized shear wave speed; V_{sv}: horizontally travelling and vertically polarized shear wave speed; Q: quality factor; ρ: density; $\delta\ln\mathrm{V}$: percentage perturbations relative to a 1-D reference model. Network abbreviations: NCEDC: Northern California Earthquake Data Center, SCEDC: Southern California Earthquake Data Center, FDSN: International Federation of Digital Seismograph Networks

coverage, FWI is still unable to recover some small-scale structures compared to traditional asymptotic methods but with more suitable data sets. For example, in Pacific Northwest, the Cascadia slab shows up as elongated narrow and strongly high-*V* anomalies in model US-SL-2014 because short-period teleseismic body wave travel time data enhances the lateral resolution of the structures at such scale. On the other hand, the FWI model Krischer18, although based on a more accurate 3-D sensitivity kernel, does not well capture the narrow high-*V* Cascadia slab due to the lack of short-wavelength teleseismic data that can sample the slab with good azimuthal and incidence angle coverage.

Besides the differences in data sets and tomographic methods, crustal models used in the seismic inversion can also lead to differences between mantle models. An accurate crustal model is critical for correctly recovering deeper structure, especially the uppermost mantle because of the trade-off between shear wave speeds in the uppermost mantle and the crust (Bozdağ & Trampert 2008; Panning *et al.* 2010). Fig. 2 shows the absolute shear wave speeds at 20 km depth for three different crustal models of GyPSuM, US.2016 and Krischer18, along with a reference 3-D crustal model, CRUST1.0 (Laske *et al.* 2013). The average shear wave speed difference amongst the crustal models within the contiguous US reaches up to 10 per cent, for example, about 3.3 km s^{-1} beneath the Pacific Northwest in model Krischer18 compared to about 3.7 km s^{-1} in model US.2016 and an average of 3.5 km s^{-1} beneath the central and eastern US in model Krischer18 compared to 3.9 km s^{-1} in model CRUST1.0. The impact of the crust and uppermost mantle on the predicted waveforms will be discussed in the following sections.

2.2 Spectral-element method and model implementation

The predictability of the selected 3-D models is evaluated by comparing the observed waveforms with the synthetic waveforms calculated by the SPECFEM3D_GLOBE solver based on the SEM (Komatitsch & Tromp 2002a, b). The SEM combines the accuracy of pseudo-spectral method and the flexibility of finite-element mesh (Komatitsch & Tromp 2002a), which honours the topography/bathymetry and any laterally varying internal discontinuities of the Earth such as the Moho, 410-and 660-km mantle transition zone discontinuities. It is more accurate in simulating surface waves than finite-difference methods which have stronger numerical dispersion issue (Robertsson 1996). The effects of Earth's ocean gravity, ellipticity, 3-D complex heterogeneity, attenuation and anisotropy on seismic wave propagation can also be accurately modelled (Komatitsch & Tromp 2002b).

The SEM mesh in this study is designed to simulate seismic waves accurately to the shortest period of 9 s. The horizontal grid spacing is 5 km between Gauss–Lobatto–Legendre points in the crust and doubled in the mantle. The computational domain is a spherical chunk from Earth's surface to the core mantle boundary, laterally spanning the entire contiguous US, Mexico and majority of Canada, with horizontal dimensions of 48° × 48° along great circles centred at (99° W, 30° N) and rotated by 30° counterclockwise (Fig. 3a) with Stacey absorbing boundary condition applied at the edges of the computational domain.

The implementation of different models in one uniform SEM mesh is challenging for a completely fair model comparison. First, the selected models have different study regions and parametrizations, which leads to unresolved regions (e.g. Mexico) and unconstrained parameters (e.g. V_p). Filling the gaps in the computational domain may bring uncertainties. Second, each model is inverted with different mesh configurations thus interpolation is required to fit in the SEM mesh. These two main obstacles make it extremely difficult to accurately compare the data predictability of all the tested models. However, for the purpose of constructing an initial model for FWI, we will focus on the compatibility of each model with the pre-defined mesh configuration for future FWI. Therefore, the models are implemented with the same mesh configuration with topography, radial anisotropy and attenuation regardless their original set-up.

The compatibility of crustal and mantle models needs special attention. Except models US.2016, Krischer18 and GyPSuM which have both crust and mantle, other models are implemented with model CRUST1.0 in the crust because we would like to test the compatibility of those mantle models with this most updated global crustal model, even if some of the global models (e.g. S40RTS

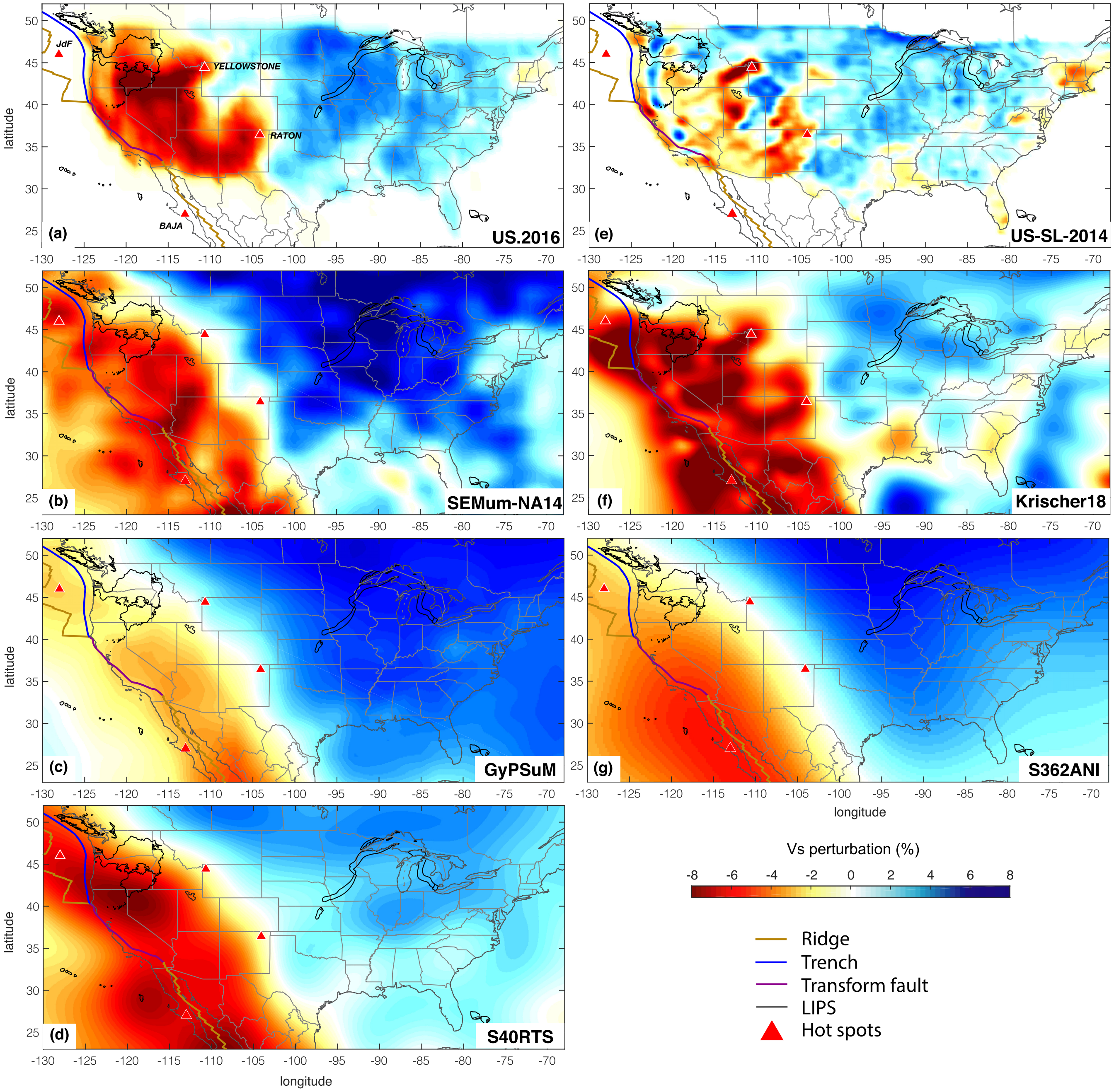

Figure 1. Comparison of seven shear wave speed models (US.2016, SEMum-NA14, GyPSuM, S40RTS, US-SL-2014, Krischer18 and S362ANI) beneath the contiguous US at 100 km depth. Shear wave perturbations are relative to 1-D reference model AK135. For display purpose, all models are interpolated on even grids with a horizontal grid spacing of 0.25°. Models US.2016 and US-SL-2014 only cover part of the map region within the contiguous US and the rest of the map is filled with zero shear wave speed perturbation. Plate boundaries and large igneous provinces (LIPS) are marked with colored lines. Red triangles denote the hot spots or volcanic regions beneath Juan de Fuca plate, Yellowstone, Raton-Clayton and Baja California (Coffin *et al.* 2005).

and S362ANI) applies CRUST2.0 for crustal correction in their inversion. For model US.2016, we implemented its own crust with their Moho by stretching the wave speeds according to the Moho and surface topography.

Some model does not constrain the *P*-wave speed. For those models, a constant V_p/V_s ratio, 1.73, is applied to assign V_p. Density ρ is assigned using the values from model AK135. The SEM mesh enables radial anisotropy to account for the models with radial anisotropy parametrization (SEMum-NA14 and S362ANI). For implementing the isotropic models, the V_{sv} and V_{sh} are assigned with the same isotropic shear wave speed V_s. The Q value is assigned from model PREM in the mantle and a constant $Q = 600$ in the crust. The implementation details for each model is described in Supporting Information S1.

2.3 Test data set

A total of 30 earthquakes are selected from the global centroid moment tensor (CMT) solution catalogue (Ekström *et al.* 2012) based on their large number of high-quality waveforms with high

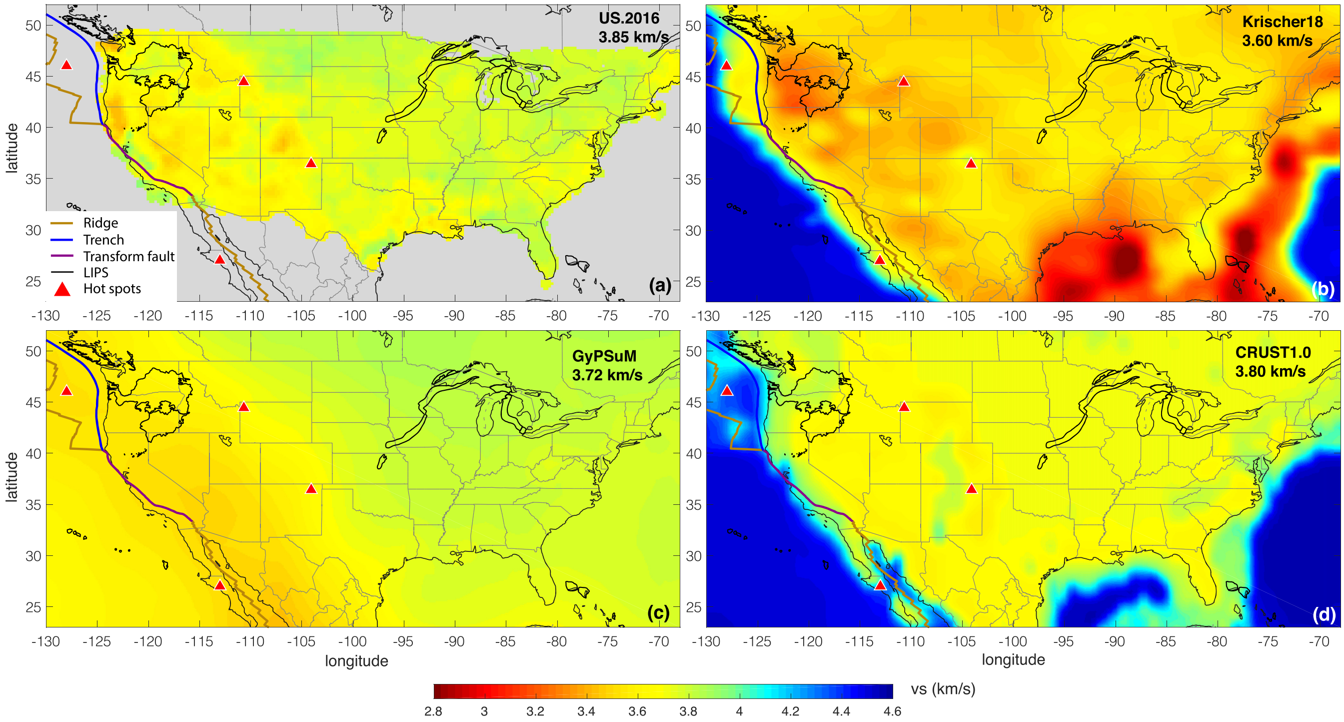

Figure 2. Maps of absolute shear wave speeds of the four selected crustal models at 20 km depth. (a) Model US.2016; (b) model Krischer18; (c) model GyPSuM; (d) model CRUST1.0. Only models US.2016, Krischer18 and GyPSuM have crustal structure provided, all the other tested models are implemented with model CRUST1.0 in the crust. Model US.2016 only covers part of the map region and the rest is filled up with grey colour (in the mesh implementation, CRUST1.0). The marked geological units are the same as those in Fig. 1.

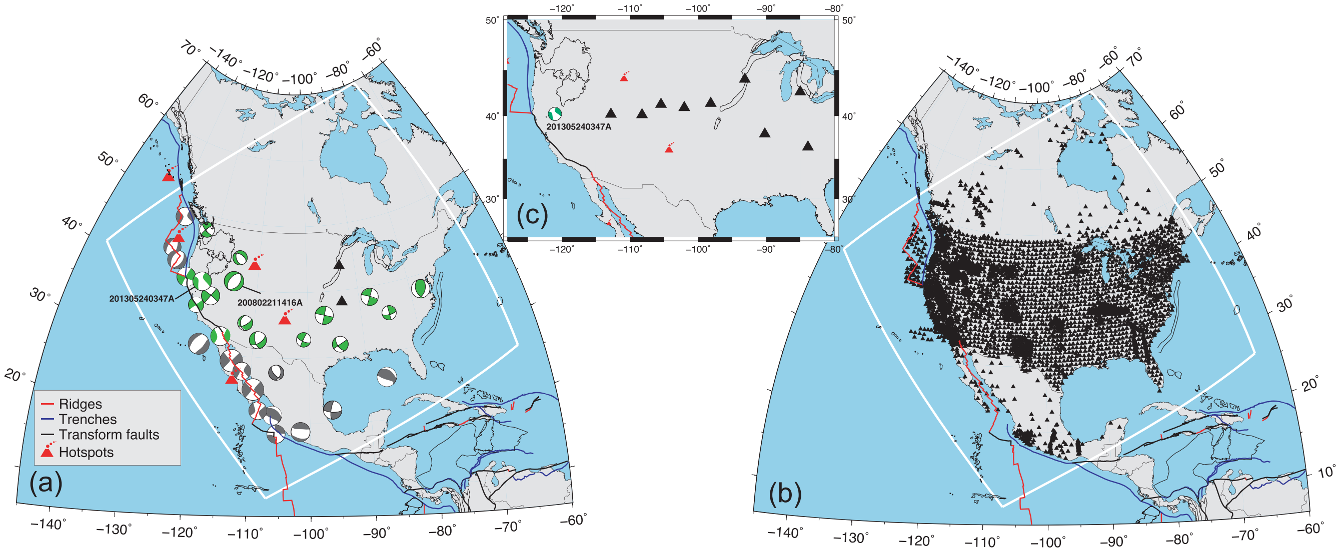

Figure 3. Event and station distribution in the simulation region. (a) 30 events and (b) all stations are used for waveform misfit comparison amongst different test models. Green coloured beachballs are contiguous US events, while dark grey coloured beachballs are other events outside contiguous US. White box outlines the simulation region. (c) The earthquake 201305240347A (M_w 5.7) for waveform comparison examples, and the stations along an approximate E-W profile with event backazimuth within 10 degrees of deviation.

signal-to-noise ratio (SNR) and representative geographic coverage of the simulation region (Fig. 3a). These events are from 2006 to 2019 with moment magnitude between 4.9 to 6.7. The depth of these events is mostly within the crust, and only two of them are deeper than 30 km. 16 are located within the contiguous US. The optimal test data set should not contain any event from data sets used for the inversion of any tested model. Otherwise, it will lead to extra bias in the data misfit. In this paper, since we are using full-waveform-based measurements and misfit functions, models US.2016, US-SL-2014, GyPSuM, S40RTS and S362ANI are less affected by the test data sets because those models minimize different misfit functions using different wave observables. Two FWI-based models, SEMum-NA14 and Krischer18, may be affected by the extra bias induced by the test data set. We used all the broad-band stations available from different data centres such as IRISDMC, SSN and CNDC, with a total number of 5820, shown in Fig. 3(b). On average, there are more than 500 stations available for each event.

To process the data, we first remove the instrument response and convert the records to displacement with a wide-band frequency taper as the pre-filter, and then check the data SNR and select all traces with SNR > 4. Then, we bandpass filter the waveforms to our frequency ranges of interest with a zero-phase fourth-order Butterworth filter. Finally, both the data and the synthetics on E and N components are rotated to the radial and tangential (*R* and *T*) components according to the backazimuth. The synthetic waveforms follow exactly the same procedures of pre-processing as the observed data.

Since some tomographic models (e.g. SEMum-NA14 and S40RTS) utilize long-period body waves starting at 40 s, we choose two period ranges of 20–40 and 40–120 s to assess the intermediate- and long-period waveform fitting of the models. The waves of 9–20 s are also considered to test the waveform fitting in shorter period range.

2.4 Misfit measurements between data and synthetics

We apply four different criteria in this study to assess the waveform fitting between the data and synthetics: frequency-dependent traveltime misfit, amplitude misfit, least-squares waveform misfit and waveform similarity measured by the NZCC. The frequency-dependent traveltime misfit for a single measurement is defined as the square of traveltime difference between data and synthetics measured by cross-correlation in the selected time window (Tromp *et al.* 2005):

$$\chi_r^T = \frac{1}{2}[T_r^s - T_r^d]^2, \tag{1}$$

where T_r^s and T_r^d are the measured traveltime of synthetics and data of a specific phase at station *r*. The amplitude misfit for a single measurement is defined as (Tromp *et al.* 2005):

$$\chi_r^A = \frac{1}{2}[A_r^d / A_r^s - 1]^2, \tag{2}$$

where A_r^s and A_r^d are the measured amplitude of synthetics and data of a specific phase at station *r*. The waveform misfit for a single measurement is defined as (Tromp *et al.* 2005):

$$\chi_r^F = \frac{1}{2}\int_{t_s}^{t_e} [s(x_r, t) - d(x_r, t)]^2 \mathrm{d}t, \tag{3}$$

where $s(x_r, t)$ and $d(x_r, t)$ are synthetic and data at the station *r* (with location x_r). t_s and t_e are the start and end time of the selected time window.

We also consider the NZCC, which best reflects both the phase match and the similarity of complex waveform shape, for example, for triplicated waveforms but without considering the absolute amplitude. It has been used as an objective function for FWI which more robustly recovers seismic structures with strong wave speed contrasts than using frequency-dependent traveltime misfit (Liu *et al.* 2016; Tao *et al.* 2017, 2018). The NZCC is defined as:

$$\mathrm{NZCC} = \frac{\int_{t_s}^{t_e} \mathbf{s}(x_r, t) \cdot \mathbf{d}(x_r, t)\mathrm{d}t}{\sqrt{\int |\mathbf{s}(x_r, t)|^2 \mathrm{d}t \int |\mathbf{d}(x_r, t)|^2 \mathrm{d}t}} \tag{4}$$

where $s(x_r, t)$ and $d(x_r, t)$ are the multicomponent synthetics within the measurement time window at station *r*. For the *P*, *SV* and Rayleigh waves, the vertical (*Z*) and radial (*R*) components are used for calculating NZCC, while for the *SH* and Love waves, only the tangential (*T*) component is used.

Table 2. Empirical surface wave speed for window selection.

Frequency range (s)	Rayleigh wave speed ($\mathrm{km\,s^{-1}}$)	Love wave speed ($\mathrm{km\,s^{-1}}$)
9–20	3.2	3.7
20–40	3.3	3.9
40–120	3.5	4.2

To make comparison fair, we use fixed time windows for different models, which are selected according to the traveltime predicted by 1-D model AK135 for body wave phases, and by constant wave speeds for surface wave phases (Table 2). For intermediate- and long-period ranges, *S* waves are merged within the surface wave train at local epicentral distances ($\Delta < 10°$). Therefore, for local epicentral distances, only *P*(Pnl) and surface wave windows are selected, while *P*, *S* and surface wave windows for $\Delta \geq 10°$ are selected. The *P* and *S* windows are selected 10 s before and 60 s after the predicted phase arrival time. On the other hand, the surface wave windows are 10 s before and 120 s after the predicted arrival time of the surface wave train. The measurement windows are then fine selected by the following criteria: (1) the signal-to-noise ratio of the data (SNR > 4) and (2) the cross-correlation coefficient of the data and synthetics (CC > 0.7), which is used in selecting FWI measurement windows (Maggi *et al.* 2009) and constructing misfit functions (Tao *et al.* 2017).

The model predictability can be represented by weighted total misfits. We apply the same categorical weighting scheme as previous FWI studies (Tape *et al.* 2010; Chen *et al.* 2015a; Zhu *et al.* 2017) to make our model assessment consistent with FWI workflow, which is suitable for FWI initial model selection. The categorical weighting separates all the measurements to six categories: body waves and surface waves on *Z*, *R* and *T* components, respectively. This scheme balances different number of measurements on each component and each category of seismic phases, that is, body and surface waves. Since the station distribution is highly biased and varies for different events (e.g. a dense local network with 10-km station spacing such as SCEDC, compared to the USArray with average station spacing of 70 km), it is important to apply a proper weighting scheme to account for the biased station distribution for each event in evaluating the overall predictability of each model. For each testing event, we applied the station weighting based on their geographical distribution (Ruan *et al.* 2019). To make the measurements of different windows comparable, we normalize the traveltime and the amplitude misfits by the standard deviation of their measurement, that is,

$$\chi^T = \frac{1}{2CN}\sum_c^C\sum_r^N W_c W_r \left(\frac{T_r^s - T_r^d}{\sigma_r}\right)^2, \tag{5}$$

$$\chi^A = \frac{1}{2CN}\sum_c^C\sum_r^N W_c W_r \left(\frac{A_r^d / A_r^s - 1}{\sigma_r}\right)^2, \tag{6}$$

where W_r is the geographical station weighting coefficient (Ruan *et al.* 2019) and W_c is the category weighting coefficient, which is the inverse of the number of all the selected measurement time windows of that category. σ_r is the estimated error of the measurement, calculated by the MEASURE_ADJ incorporated in the SPECFEM3D_GLOBE code package (Komatitsch *et al.* 9999). *C* and *N* are the numbers of total categories and stations, respectively. In the waveform and NZCC measurements, we only apply the categorical and geographic weighting:

$$\chi^F = \frac{1}{CN}\sum_c^C \sum_r^N W_c W_r \chi_r^F \tag{7}$$

$$\chi^{\mathrm{NZCC}} = \frac{1}{CN}\sum_c^C \sum_r^N W_c W_r (1 - \mathrm{NZCC}) \tag{8}$$

where W_r and W_c are the geographical and categorical weighting coefficients, respectively.

The uncertainty of source parameters also has impact on the waveform fitting measurements. Here, we apply a combination method of CMT3D (Liu *et al.* 2004) and the grid-search of Rayleigh wave spectra (Jia *et al.* 2017) to re-invert for the moment tensor and event depth (Supporting Information S2 and Fig. S1). The combination of the two methods has higher sensitivity of event depth. The example of earthquake event with global CMT event ID of 200802211416A shows a slight depth decrease and a better amplitude misfit for Rayleigh waves. There will be extra bias introduced by source parameter re-inversion. For example, the AK135+CRUST1.0 model applied in the source re-inversion will make the source parameters more compatible with this particular model, as well as models with CRUST1.0 as crustal model. Nevertheless, the waveform predictability also increases for the example event (200802211416A) in a different model (US.2016) partially indicates the source inversion does improves the accuracy of source parameters.

3 RESULTS

3.1 Waveform comparison of different seismic models

To visualize the waveform fitting, we choose an earthquake event 201305240347A (M_w 5.7) and stations located towards east in the azimuth range of $90 \pm 10^\circ$ (Fig. 3c, vertical cross-section: Fig. S2, Supporting Information). We demonstrate waveform comparisons of intermediate-period shear waves (20–40 s, Fig. 4) and long-period surface waves (40–120 s, Fig. 5) in vertical and tangential components. The intermediate-period shear waves merge with the surface waves within epicentral distance ranges of 10° (Fig. 4), therefore, only surface wave windows are plotted for the local epicentral distance stations. The turning depth of the *S*-wave ray ranges from 35 to 816 km, which is mostly sensitive to the upper mantle.

All the models fit regional *SV* and *SH* phases well (Fig. 4). Models derived with full-waveform tomography, for example, Krischer18 and SEMum-NA14 seems to have better waveform fitting and smaller traveltime misfit on vertical components. On the other hand, models with radially anisotropic constraints, for example, S362ANI and SEMum-NA14 performs better on tangential components. The models all have a larger phase shift for local Rayleigh waves but performs better for local Love waves. In general, all the models are consistent in well predicting the waveforms in the period range of longer than 20 s, and are compatible with the realistic mesh configurations.

Surface waves in the long-period range of 40–120 s are most sensitive to the upper-mantle structure. Here, Rayleigh waves on vertical components are well predicted by all the tested models (Fig. 5) and amongst which, model US.2016 has the smallest Rayleigh wave phase misfit. However, models AK135, US.2016 and US-SL-2014 have relatively large phase misfit of the Love waves. Interestingly, global models S362ANI, and even S40RTS which does not have radial anisotropy constraint, manifest a better Love wave fitting which is partially due to the better compatibility of crustal and mantle models implemented (see Section 4). This observation suggests that radial anisotropy in the upper mantle of the contiguous US and surrounding regions still needs to be refined.

Waveforms in the short-period range of 9–20 s are most sensitive to small scale heterogeneities in the crust. However, relatively large body and surface wave misfits for all the models in 9–20 s are observed (Supporting Information S3, Figs S3 and S4). Currently, none of the models can predict the waveform complexities of the shortest period around 9 s. For body waves, models US.2016, S40RTS and US-SL-2014 have a slightly better waveform fitting (Fig. S3, Supporting Information). The short-period surface waves manifest strong coda reverberations (Fig. S4, Supporting Information), which may be related to reverberations triggered by the deep sedimentary basins (e.g., Forest City, Cherokee and Illinois; Coleman & Cahan 2012, Fig. S2, Supporting Information). The small-scale heterogeneities in the shallow subsurface also need further refinement.

We demonstrate the impact of different crustal models to the intermediate-period (20–40 s) waveforms in Fig. 6. The earthquake event 200802211416A (M_w 6.0) recorded by one global standard seismic network station IU.CCM with epicentral distance 18° is used. Three different crustal models, CRUST1.0, CRUST2.0 and US.2016 are implemented along with the same mantle model S40RTS. All the models predict *P* and *SH* waves well, while model S40RTS with CRUST2.0 has smaller waveform misfits. For SV and Rayleigh waves, S40RTS+US.2016 has the best waveform fitting, while for Love waves, S40RTS+CRUST1.0 has the best prediction. This observation suggests that the original compatible crustal and mantle models (e.g. CRUST2.0 for S40RTS) generally predicts the same types of data used in their inversion, but are not optimal for the other types of data. A crustal model with higher resolution (e.g. CRUST1.0) or with short-period Rayleigh wave dispersion constraints (e.g. US.2016) has a visible improvement on the waveform fitting of certain seismic phases such as *SV* and Rayleigh waves.

3.2 Statistical result of waveform similarity and misfit

Statistical analysis helps us assess the compatibility of the models with the contiguous US mesh configuration. First, traveltime shift histograms directly indicate the mean and deviation of each model (Fig. 7). The positive or negative traveltime indicates advance or delay of the synthetics compared to the observations, implying that the wave speed models are either faster or slower compared to the ground-truth. We observed that models S40RTS and S362ANI have the minimum standard deviation in all three period ranges. The two global models completely cover the entire study region and are free from the bias introduced by merging different models. Models GyPSuM, Krischer18 and US.2016 have the lowest mean traveltime error in 9–20, 20–40 and 40–120 s, respectively. All the models have a negative mean traveltime shift in 9–20 and 40–120 s, while only GyPSuM and Krischer18 have positive traveltime shift in 20–40 s period range. The observed biased shear wave traveltime misfit is likely due to the surface topography effect. The top layer of each model is stretched to fit the surface topography above the sea level in the contiguous US, but this layer usually have faster wave speed than a realistic near-surface sedimentary layer. Measurements with only body or surface waves share similar statistical results (Figs S5–S8, Supporting Information). *SH* wave speed for all the models is systematically slower (Fig. S6, Supporting Information), while the Love wave speed (Fig. S8, Supporting Information) shows less systematically biased distribution, indicating the mantle

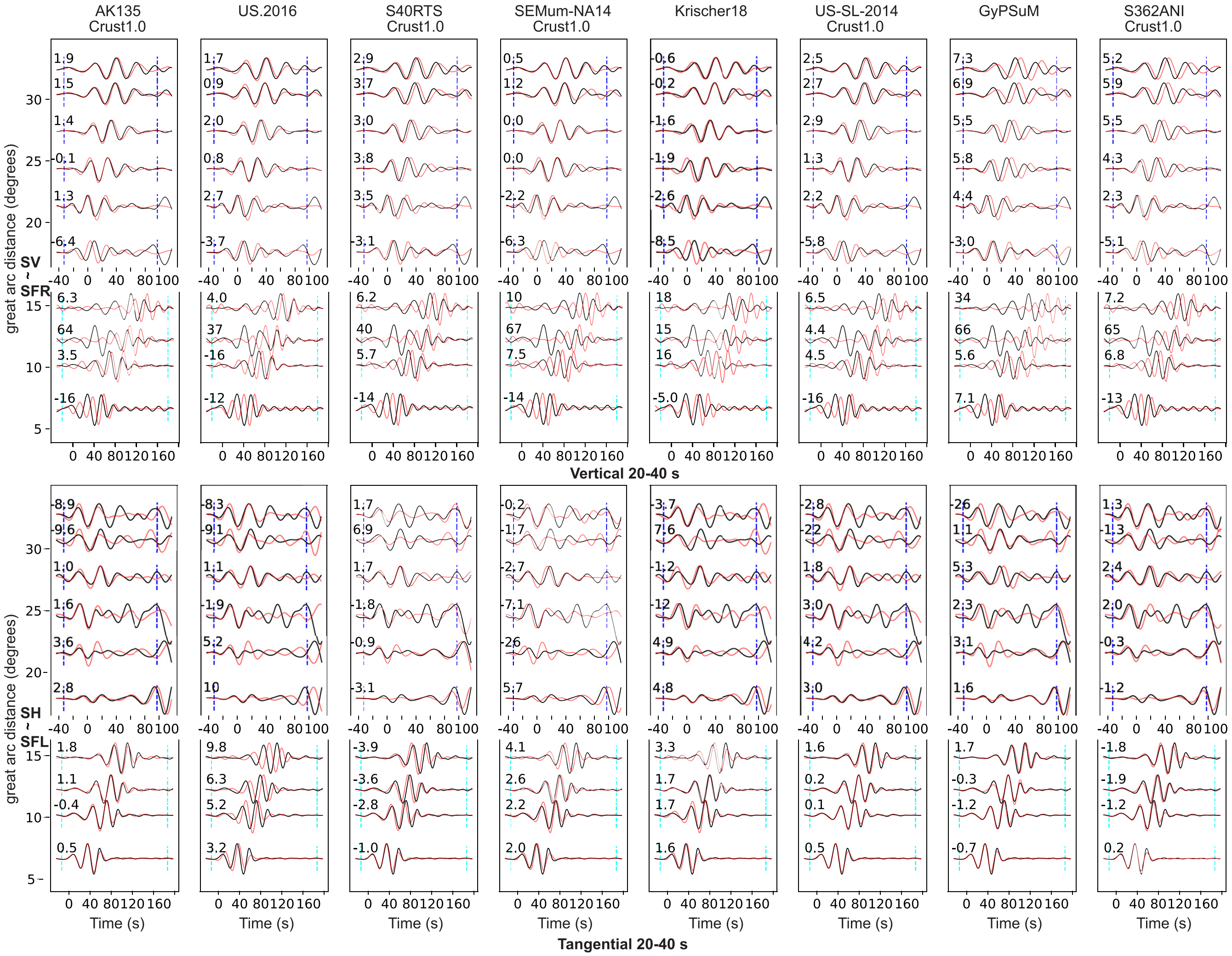

Figure 4. Waveform comparison for intermediate-period shear wave (20–40 s) on vertical and tangential components. Traces are shown in Fig. 3, aligned with reduced time reference to the *S*-wave arrival time predicted by AK135. Black and red lines are the observed and synthetic waveforms, respectively. For local traces, surface wave takes over *S*-wave phases. Blue and cyan dashed lines mark the shear and surface wave measurement windows, respectively. Numbers mark the cross-correlation measured traveltime difference between synthetics and data.

radial anisotropy need further refinement (Supporting Information S4). Amongst these models, models SEMum-NA14 and S362ANI have better performance in predicting seismic waves on different components, probably due to the radial anisotropy is constrained in these two models.

Besides the statistical analysis, we examine the averaged traveltime shift of all the available events at each station, which shows the waveform fitting in different geographic regions. Fig. 8 shows the shear wave traveltime misfit in the intermediate (20–40 s) period range for all the tested models. Generally, the absolute traveltime misfit in the western US is slightly larger than the eastern US, indicating that the western US has more complex and unresolved structures. The Rocky Mountain and Plateau region has relatively large shear wave misfit while for the Great Plain region relatively small, possibly due to the complex topography effects in the Rocky Mountain and Plateau region. The global models S40RTS, GyPSuM and S362ANI have a relatively small misfit in the Eastern US than the other models, which may indicate that these global models capture the average large-scale structures in the Eastern US well.

We examine the compatibility of each model with our FWI mesh configuration by a variety of misfit functions (Fig. 9). The traveltime and NZCC misfits have a similar trend of model ranking, which is because of the NZCC misfit also measures the phase difference which is similar to the traveltime misfit. Models S40RTS, S362ANI and US.2016 are the top three models with minimal overall traveltime and NZCC misfit in 20–40 and 40–120 s period ranges, while in 9–20 s period range, model AK135 becomes one of the top three instead of US.2016. This result is counterintuitive yet understandable because most of the 3-D models are inverted by intermediate-to long-period waves (20–40 s) and are biased due to model implementation and interpolaton. Global models constrained by both traveltime data (short period) and surface wave dispersion data (long period) has the smallest misfit of phase for both body and surface waves in different frequency ranges. Measurements with body or surface waves share similar statistical results as the ones of all the seismic phases combined (Figs S9 and S10 , Supporting Information).

For the amplitude and waveform misfits with long periods, a similar trend of model ranking as traveltime and NZCC misfit is

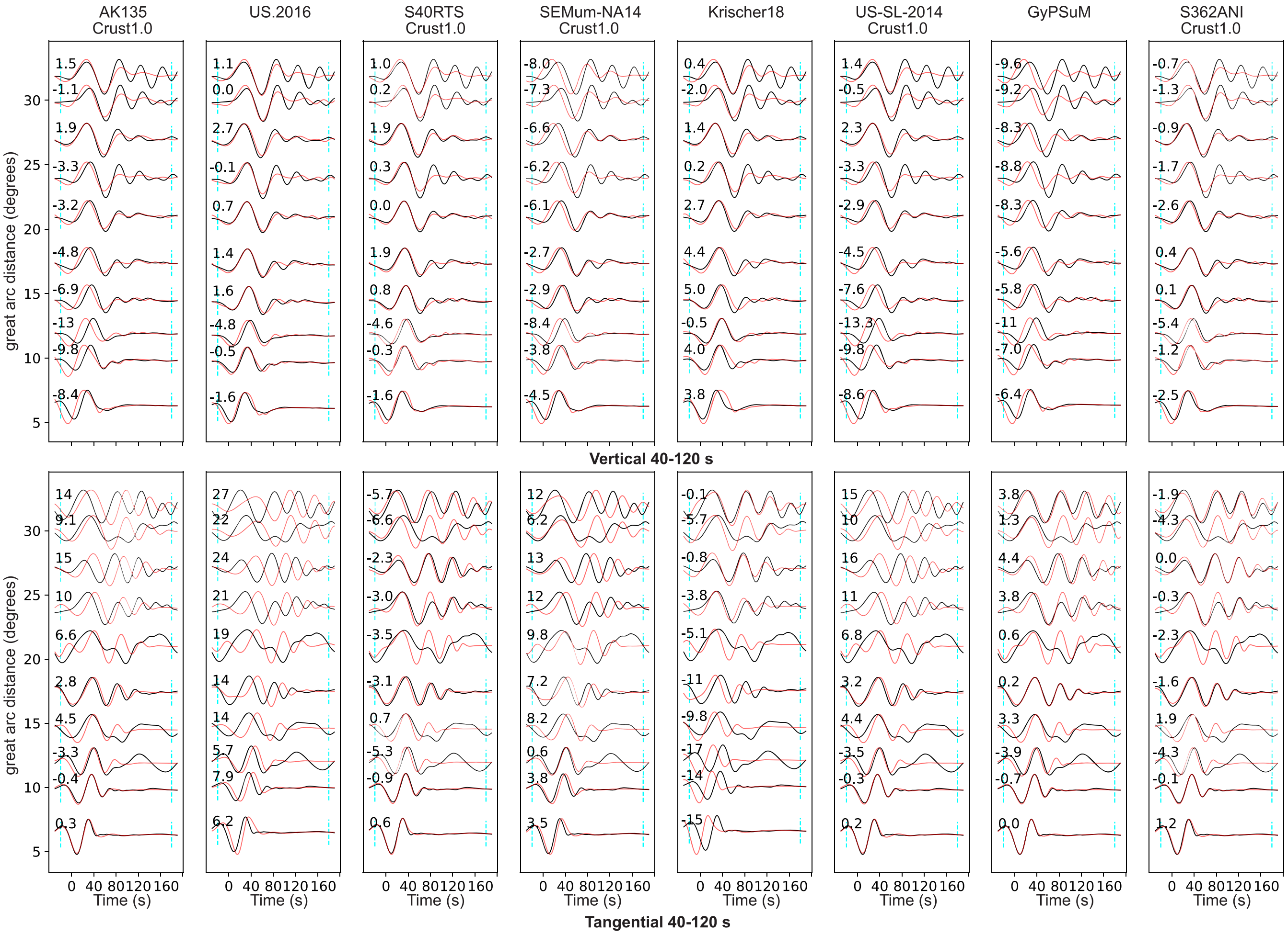

Figure 5. Waveform comparison for long-period surface wave (40–120 s) on vertical and tangential components. Traces are shown in Fig. 3, aligned with the empirical arrival time of Rayleigh or Love waves calculated by empirical surface wave speeds in Table 2. Cyan dashed lines mark the surface wave measurement windows. Numbers mark the cross-correlation measured traveltime difference between synthetics and data.

observed. However, in the short-period range, the amplitude and waveform misfits are more unpredictable. The amplitude and waveform misfits may not be very indicative of the model predictability because none of the tested models are inverted by minimizing absolute amplitude or waveform misfits. The short-period surface waves are not predicted by all the models, indicating that none of them has a good constraint of the very shallow subsurface structure such as the sedimentary basins. The long-period surface waves are less influenced by the strong- and small-scale heterogeneities in the shallow depths, therefore, the amplitude and waveform misfits are more indicative in assessing the model predictability for long periods. Further refinement for near-surface small-scale heterogeneities is still needed for seismic wave speed models of contiguous US and surrounding regions.

Using NZCC, we can determine the percentage of windows selected for measurement from all the possible windows. It is an important criterion that directly indicates the number of usable measures we can obtain in the first iteration of an FWI, thus indicative for initial model predictability. Here, we plot the percentage of measurement windows with NZCC > 0.7 for all the models in three period ranges and six categories (Fig. 10). To make the comparison fair, we examine only contiguous US earthquakes including events off coast western US because models US.2016 and US-SL-2014 only have contiguous US part resolved. For the short-period range (i.e. 9–20 s), models S362ANI, S40RTS and GyPSuM are the three models with higher percentage of usable measurement windows of body waves, while model US.2016, US-SL-2014 and Krischer18 have higher percentage of usable windows of Rayleigh waves. For love waves, model AK135+CRUST1.0 predicts the waveforms better than model US.2016, which indicates that CRUST1.0 is more suitable for *SH* waves in the crust. For the long-period range (40–120 s), models S40RTS, S362ANI and SEMum-NA14 are the top three models with the highest percentages of usable windows for all six categories, which further confirms that the predictability of certain types of waves is highly dependent on the data used in the inversion, for example, the long-period waveforms used in these three models. In the intermediate-period range (20–40 s), models S40RTS and S62ANI are amongst the best three models with the highest percentages of NZCC > 0.7 measurement windows for all the categories, while SEMum-NA14 and Krischer18 also predict well for some categories. The overall percentage of good measurements increases with increasing periods.

The model predictability varies with the epicentral distance in each category (Fig. 11). For surface waves, the predictability of all the models decays with increasing epicentral distances, which

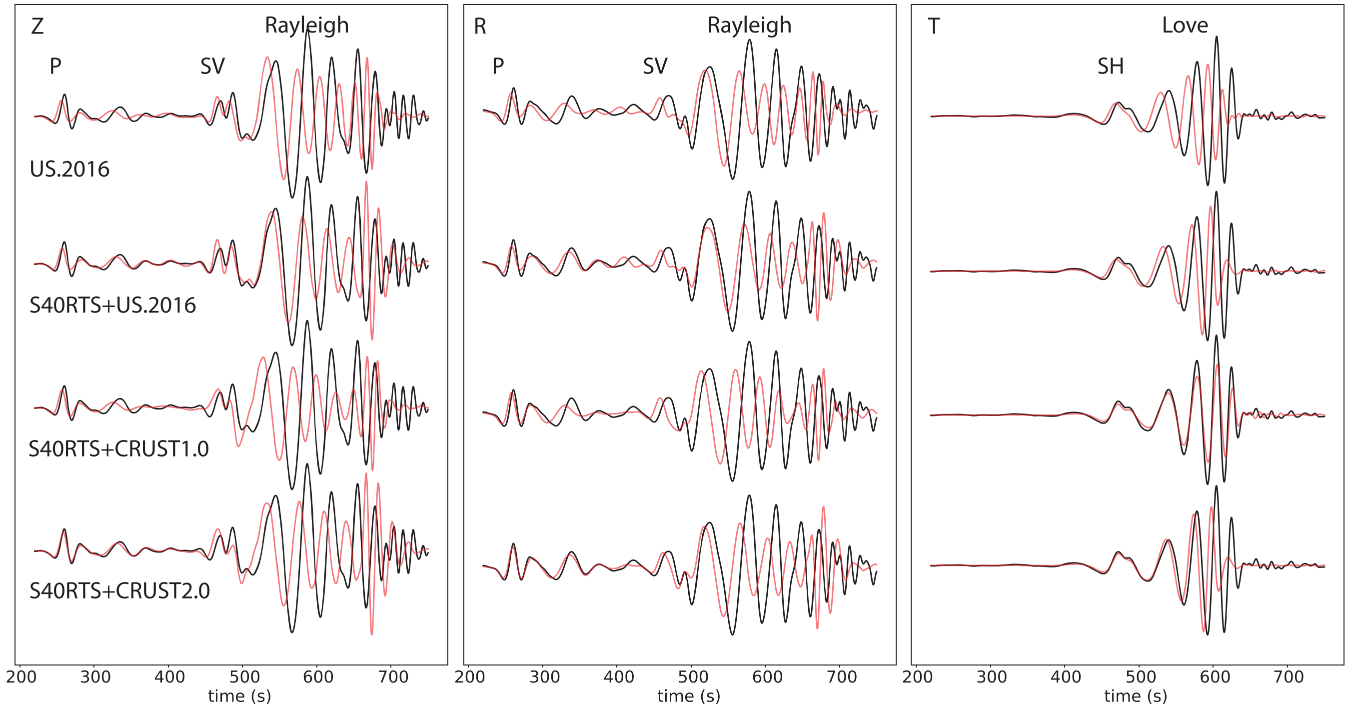

Figure 6. Waveform comparison of the same mantle model S40RTS with different crustal models. Event: 200802211416A (M_w 6.0); station: IU.CCM. Epicentral distance: 17.9°. Red and black lines are synthetic and observation waveforms, respectively.

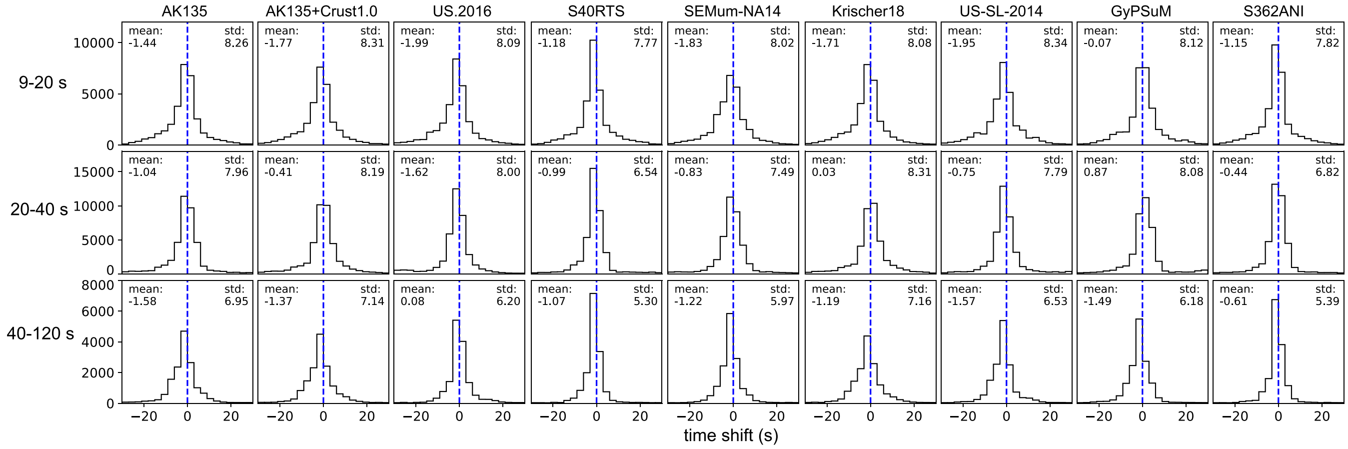

Figure 7. Traveltime shift distribution histograms for all the measurement windows. Rows upper to lower: 9–20, 20–40 and 40–120 s and panels left to right: different models.

may be contributed by the small-scale heterogeneities in the crust and uppermost mantle. These small-scale heterogeneities are not well constrained by the current models thus complex surface wave dispersion at increasing epicentral distances cannot be fully reproduced. Model US.2016 performs the best for short-period (9–20 s) Rayleigh waves in all the epicentral distances, indicating a relatively better constrained shallow subsurface structures. Models with CRUST1.0 (S40RTS, US-SL-2014 and SEMum-NA14) performs better in fitting short-period Love waves, which further confirms that CRUST1.0 serves as a good model for *SH* wave speeds in the crust of the contiguous US and surrounding regions. Models S40RTS and S362ANI are amongst the best-fitting models in periods greater than 20 s, while models Krischer18 and SEMum-NA14 also show good predictability especially at larger epicentral distances. For body waves, models S40RTS and S362ANI generally outperforms other models, especially at large epicentral distances. We also noted that model AK135 predicts 9–20 s shear waves at small epicentral distance well, however the composite model with CRUST1.0 and AK135 worsens the waveform fitting, which is consistent with the previous study on that adding 3-D crust does not necessarily improves the data fitting for 1-D models (Bozdağ & Trampert 2010).

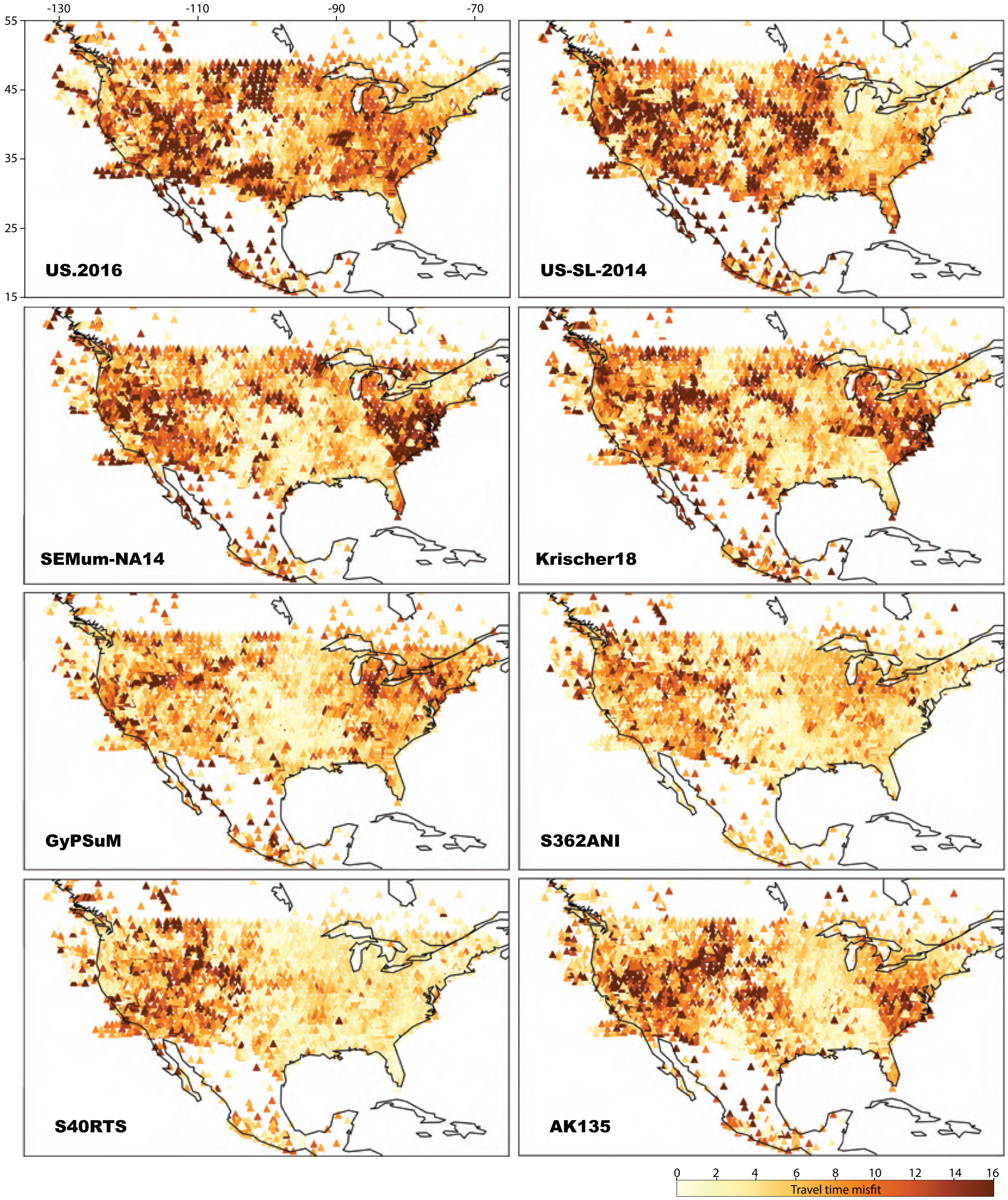

Figure 8. Averaged shear wave traveltime misfit at each station for all the testing events. Stations are colour coded by traveltime misfit value in 20–40 s. Each panel are different models.

4 DISCUSSION

4.1 Uncertainties and assessment of the data misfit for model comparison

Uncertainties of the data misfit come from various aspects. First, the incompleteness of model parameters and the model implementation process to composite different models lead to extra bias in the waveform simulations. An example is that a model with different crust and mantle patched up together, synthetic waveforms represent the integration of two models along the ray path. Besides, artificial boundaries, interpolation and smoothing schemes also creates artefacts and bias in the synthetic waveforms. Therefore, assessing the model predictability based on the waveform comparison result need to be carefully discussed. Body waves in regional epicentral distances (10°–30°) are sensitive to the upper-mantle structure, while in local epicentral distances sensitive to the crustal structure, for example, Crust1.0. Therefore, it is important to analyse the NZCC statistics by taking into account of epicentral distances (Fig. 11), the waves of which are sensitive to models at different depth ranges.

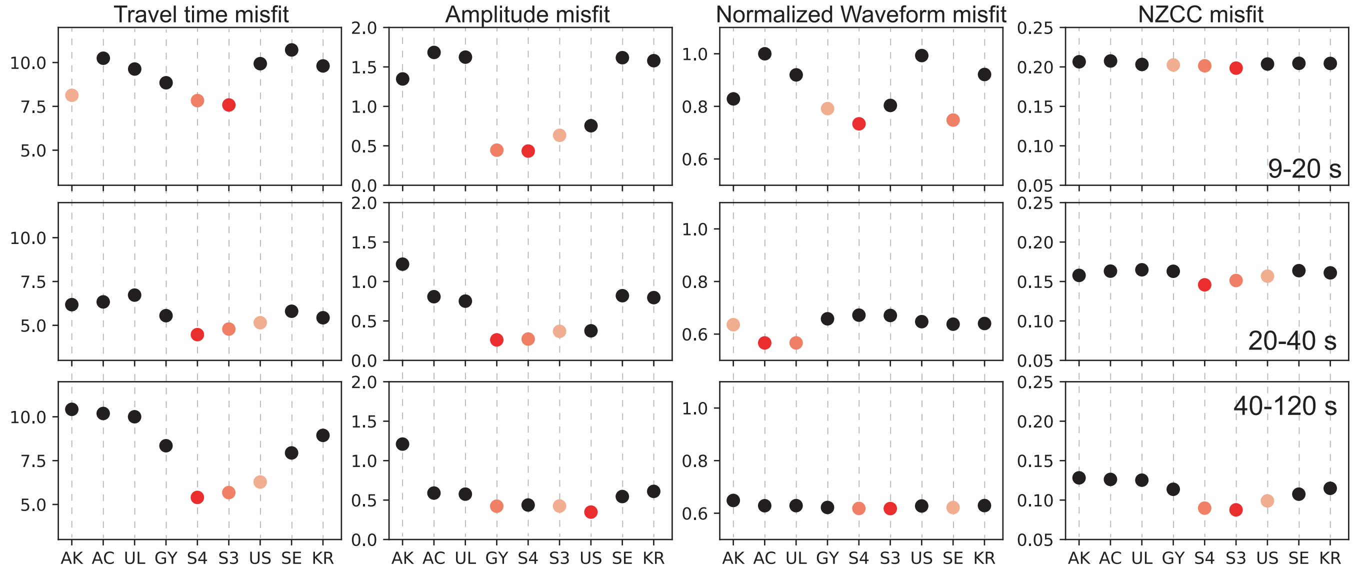

Figure 9. Four types of misfit for contiguous US events in three period ranges. Rows upper to lower: 9–20, 20–40 and 40–120 s; panels left to right: traveltime, amplitude, waveform and zero-lag CC misfits, respectively. First three models with minimum misfits are marked with different reds. The *x*-axis marks are for different models: AK: AK135, AC: AK135+CRUST1.0, UL: US-SL-2014, GY: GyPSuM, S4: S40RTS, S3: S362ANI, US: US.2016, SE: SEMum-NA14 and KR: Krischer18. Models UL, S4, S3 and SE are implemented with CRUST1.0 on top.

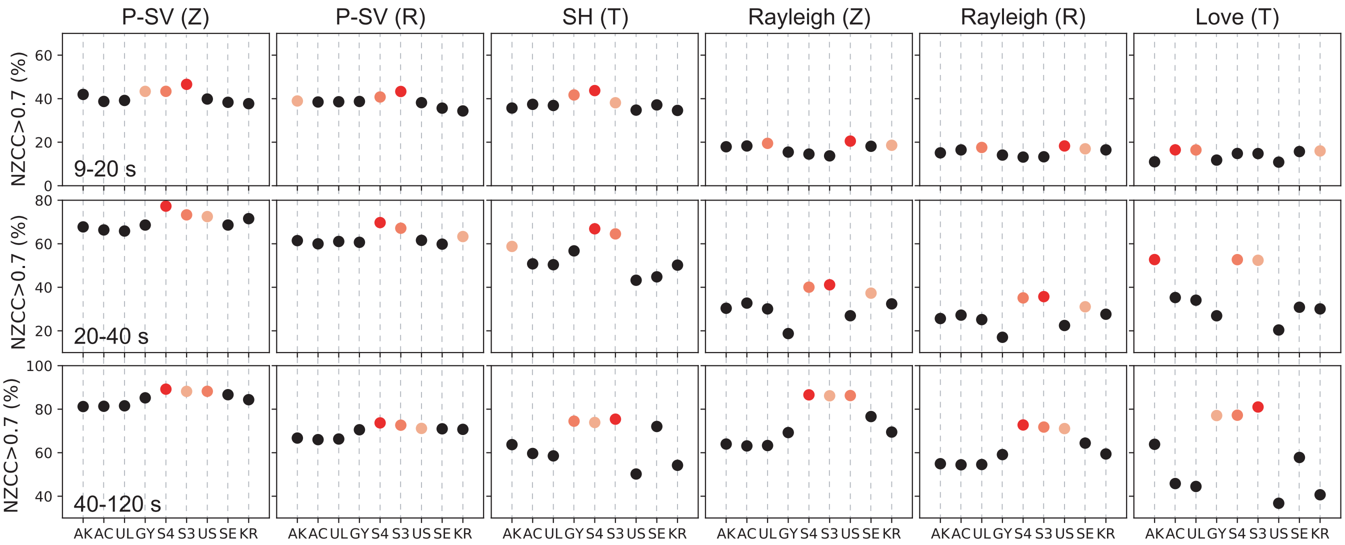

Figure 10. Model predictability defined by the percentage of NZCC > 0.7. Rows upper to lower: 9–20, 20–40 and 40–120 s; panels left to right: six categories (*P–SV Z*, *P–SV R*, *SH T*, Rayleigh *Z*, Rayleigh *R* and Love *T*). First three models with maximum percentage of NZCC > 0.7 measurements are marked with different reds. The *x*-axis marks are for different models: AK: AK135, AC: AK135+CRUST1.0, UL: US-SL-2014, GY: GyPSuM, S4: S40RTS, S3: S362ANI, US: US.2016, SE: SEMum-NA14 and KR: Krischer18. Models UL, S4, S3 and SE are implemented with CRUST1.0 on top.

The data sets used in the inversion of each model determine the data fitting in each category. For example, model US.2016 with short-period Rayleigh wave dispersion recorded by USArray significantly improves the waveform fitting of 9–20 s Rayleigh waves, indicating a better isotropic shear wave speed model in the crust. FWI models Krischer18 and SEMum-NA14 constrained by long-period (30–40 s) body and surface waves, are able to predict long period (40–120 s) and even intermediate-period (20–40 s) validation data sets. The FWI approach maximizes the information extracted from the seismic waveforms, which may have subwavelength resolution (van der Kruk *et al.* 2015). Models with radial anisotropic constraints, that is, SEMum-NA14, S362ANI and Krischer18, have better predictability of *SH* waves. Especially, model CRUST1.0 predicts both the *SH* body and Love waves, possibly because of the the V_{sh} wave speed is well constrained by both passive source and active survey data.

It is notable that global models (S40RTS, S362ANI and GyPSuM) perform well in terms of predicting phase related observables (i.e. traveltime and NZCC) in all three frequency ranges, even though they are not resolving small-scale heterogeneities. It is reasonable because all those global models are constrained by mutiple data sets, including traveltime, long-period body wave and surface wave dispersion data. The body wave traveltime, although based on ray-theory approximation and suffering from wavefront healing

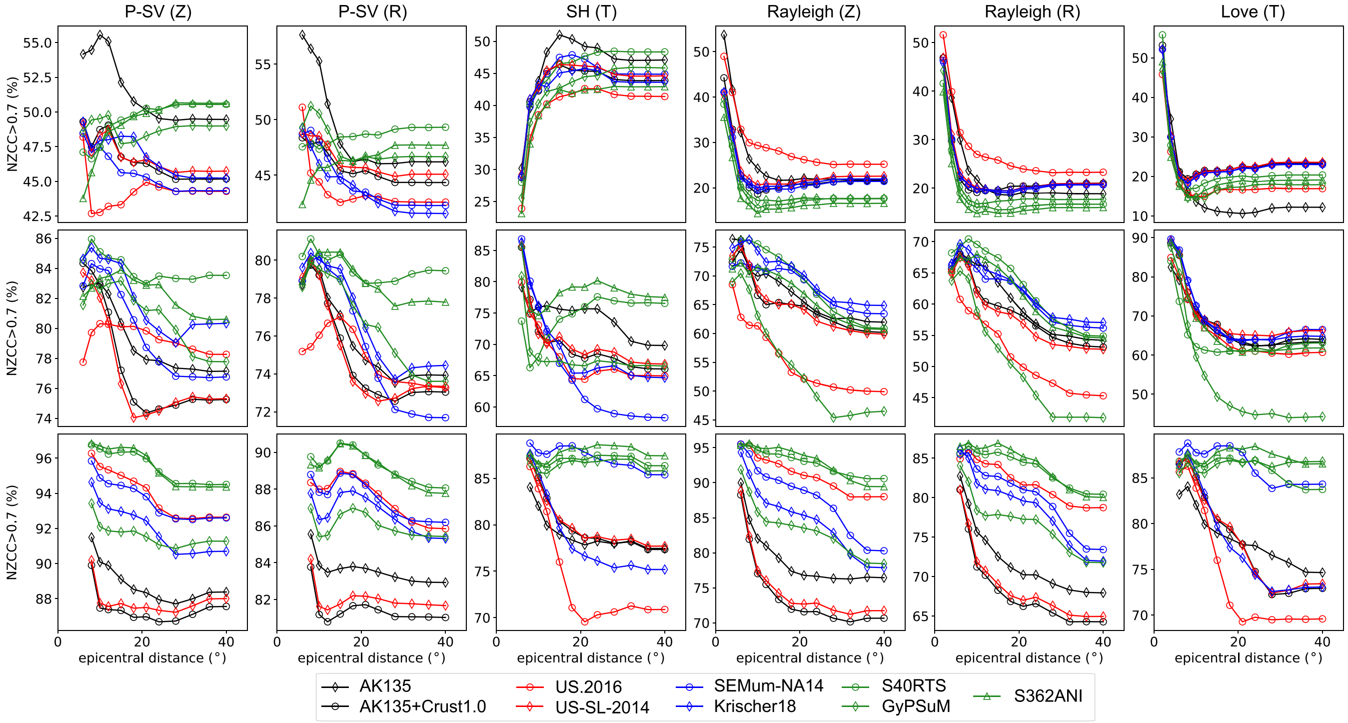

Figure 11. Model predictability versus different epicentral distances. The percentage of measurements with NZCC > 0.7 within certain epicentral distances are plotted for different seismic phases in six categories (columns left to right: *P–SV Z*, *P–SV R*, *SH T*, Rayleigh *Z*, Rayleigh *R* and Love *T*) in different period ranges (rows top to bottom, 9–20, 20–40 and 40–120 s). Higher percentages indicate better model predictability.

effect that reduces the amplitude of the wave speed anomaly thus lowers the resolution (Montelli *et al.* 2004), still has the ability to predict the phase of seismic waves in even shorter period range. The relatively evenly distributed earthquake and station locations in global model inversions may also help to balance the sensitive kernels of different geographical regions and different depths, which helps reduce the statistical bias of the model. This observation indicates that combining unbiased multiple measurements and data sets are critical for seismic wave speeds inversion. For a regional study, special attention should be paid to the possible unevenly distributed source and stations and a proper weighting scheme should be applied to mitigate the bias.

Since all models assessed are inverted from the phase (traveltime, dispersion, etc.), it is reasonable that the absolute amplitude and L2 norm of the waveform misfits are not well minimized yet, resulting in the unstable testing result for amplitude and waveform misfit comparison. Besides, the model attenuation also influences the absolute amplitude and waveforms, but is not yet constrained by any of the tested models. Sedimentary basins may produce strong reverberations which lead to complicated waveforms which are not predicted. Radial anisotropy is also not well constrained except for the two models S362ANI and SEMum-NA14. Therefore, a further model refinement for the contiguous US and surrounding regions aiming at short wavelength, small heterogeneity and radial anisotropy in crustal and upper mantle is necessary. Since we still observe discrepancies of data and synthetic waveforms in long periods, it is important to start from long-period waves to refine large-scale structures.

To conclude, in this realistic 3-D mesh configuration of the contiguous US and surrounding regions, models S40RTS and S362ANI have the best overall performance in predicting both the body waves and long-period surface waves, which may be benefitted from high-quality and spatially balanced global measurements as well as multiple phases sensitive to both the upper- and lower-mantle structure. Model US.2016 best predicts the Rayleigh waves, especially in the short-period range. However, it performs not as good as the S40RTS+CRUST1.0 in predicting the SH waves which possibly due to the limited depth (150 km) resolved and lacking Love waves in the inversion data set. Models SEMum-NA14, GyPSuM and Krischer18 are also good at predicting long-period waveforms. Especially, model SEMum-NA14 performs the best in predicting short epicentral distance *SH* and Love waves in 40–120 s, indicating the V_{sh} is well constrained in this model. For the crust, US.2016 does the best in predicting *SV* and Rayleigh waves while CRUST1.0 performs better than US.2016 in predicting *SH* and Love waves, which suggest that the crust requires radial anisotropy to better predict the data on different components.

4.2 Initial model construction for FWIs

Although it is difficult to evaluate the models because of the uncertainties in model implementation and in model compatibility between composite models, the model predictability is still meaningful for finding out the compatibility of these models with a pre-designed realistic mesh configuration (including attenuation, topography, gravity, etc.) that will be used for further FWI model refinements. A model with better data fitting and predictability makes it a good candidate for the initial model. However, more aspects apart from data-synthetics fitting need to be carefully considered to help constructing a better initial model for further FWIs.

The crustal model has a significant influence in model predictability. It is reported that frequency-dependent traveltimes measured in long periods, although mostly sensitive to mantle structure, are

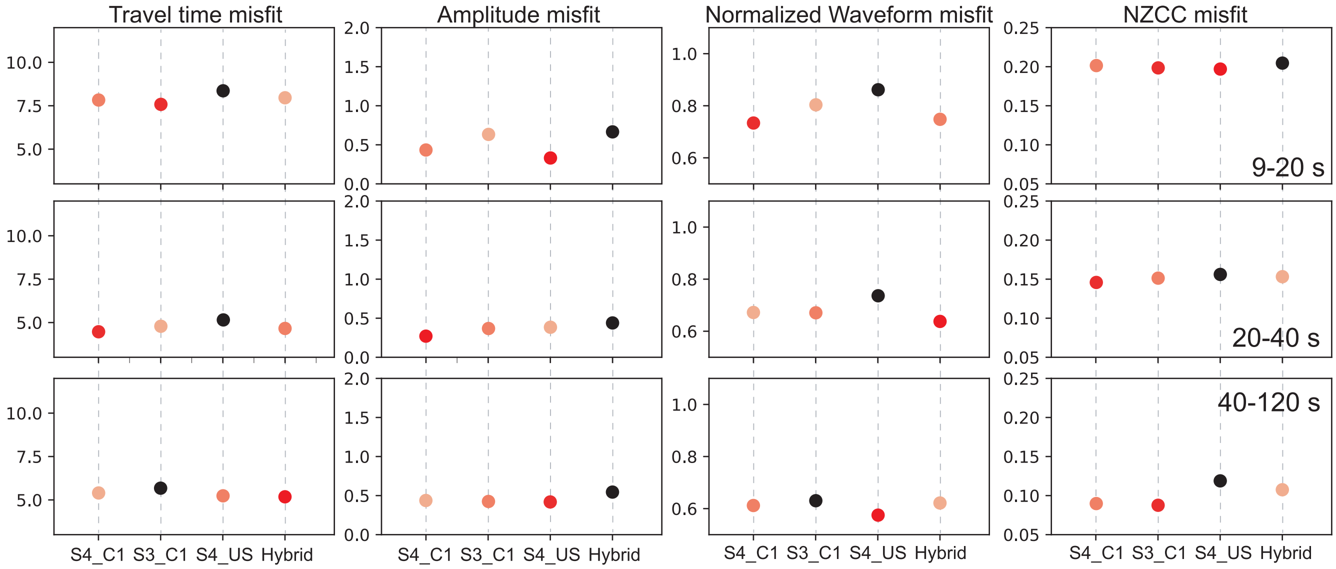

Figure 12. Four types of misfit for contiguous US events in three period ranges. Rows upper to lower: 9–20, 20–40 and 40–120 s; panels left to right: traveltime, amplitude, waveform and zero-lag CC misfits, respectively. First three models with minimum misfits are marked with different reds. The *x*-axis marks are for different models: S4_C1: S40RTS mantle with CRUST1.0; S3_C1: S362ANI mantle with CRUST1.0; S4_US: S40RTS mantle with US.2016 crust; Hybrid: hybrid model with S40RTS mantle, US.2016 crust for SV and CRUST1.0 for SH.

seconds different from the ray-theory predictions, which is related to the crustal effects (Ritsema *et al.* 2009). Therefore, in further FWI refinement, an accurate initial crust model, especially with detailed constraints of the shallow subsurface structure, is critical in precisely recover the wave speed of the deeper interior of the Earth. The compatibility of crustal and mantle models is another important issue, reported by Bozdağ & Trampert (2008), Ritsema *et al.* (2009), Panning *et al.* (2010) and Lekić & Romanowicz (2011) in terms of combining different crustal and mantle models. For example, model S40RTS shows a slightly better compatibility with CRUST2.0 compared to CRUST1.0 and crustal model from US.2016 (Figs S11–S12 and Supporting Information S5) in terms of traveltime misfit and NZCC. It is reasonable because model S40RTS uses CRUST2.0 for the crustal correction (Ritsema *et al.* 2011). However, Crust1.0 is still more suitable for the initial model because it has more seismic constraints and better resolution than CRUST2.0. Moreover, the crustal model from US.2016 that combines short-period Rayleigh wave and receiver functions greatly improves the seismic constraints of the shallow subsurface SV wave speeds in contiguous US. The further FWI refinement will benefit from a better resolved crust.

Attenuation not only affects the absolute amplitude, but also causes phase shift which leads to traveltime shift and waveform change. However in intermediate-period ranges, the attenuation induced traveltime shift is relatively small in terms of waveform (Tao *et al.* 2018) and statistics of misfits (Figs S13–S14 and Supporting Information S6). In this paper and our further FWI refinements, we use a hybrid Q model with $Q_\mu = 600$ in the crust and Q_μ from PREM model in the mantle. Nevertheless, the ultimate goal is to combine the measurement of absolute amplitude to invert for a better Q model with wave speeds model simultaneously using FWI (Zhu *et al.* 2013).

When selecting an initial model for FWI, the choice between 3-D model with high-predictability and 1-D reference model is debatable. 1-D models does not bring in any prior wave speed anomaly patterns to the inversion, while a high-resolution 3-D model with high waveform predictability can provide more initial measurements when the FWI starts from intermediate periods. Our tests show that the initial model selection depends on the starting frequency range of the FWI. 1-D reference models might not be a good choice if starting from intermediate period (20–40 s) since the initial misfit is high and the percentage of high CC measurement windows is limited. Implementing a 3-D crust on top of a 1-D mantle model probably does not improve the initial data fitting. Our observations suggest the commonly used FWI starting model S362ANI is nearly optimal in long- to intermediate-period ranges. The global 3-D mantle model S40RTS also outperforms other models in our FWI mesh configuration to invert seismic waves longer than 20 s period.

Since there are fewer earthquake events in the central and eastern US, there will be very few short epicentral distance ray paths which senses the shallow subsurface in the crust. For an FWI work involving intermediate-period waves, the surface waves are also less sensitive to the shallow subsurface structures. Therefore, it is important to get the crustal model, especially the shallow part, preconstrained with an initial crustal model that can already predict the short-period surface waves and shallow-depth turning body waves. Regional models of the contiguous US such as US.2016 captures the local structures especially the shallow subsurface *SV* wave speeds, which makes US.2016 a good candidate model for the SV wave speed model of the crust. CRUST1.0 better predicts *SH* waves than US.2016, which makes it a better candidate for the *SH* wave speed model in the crust.

Integrating the above considerations, we build a hybrid model combining surface-wave-tomography-constrained crust (i.e. US.2016) for V_{sv} and CRUST1.0 for V_{sh}, and global model (i.e. S40RTS) for the mantle. This hybrid model performs better in terms of the initial waveform fitting (Fig. 12), and combines the best crustal constrain in the contiguous US region up to date, which is suitable for better constraining the upper-mantle structure in FWI model refinements.

5 CONCLUSION

The initial model selection for FWI is a significant yet not well-constrained question. By analysing the traveltime misfit, NZCC and the percentage of high waveform similarity measurement windows, we are able to find out the compatibility of various community shear wave speed models with the pre-designed SEM mesh configuration in the contiguous US and surrounding regions. An optimal initial model will show a high predictability for good initial data misfits and a high percentage of usable measurement windows for good initial data coverage. We conclude that each model works best for different aspects of modelling. Based on our test in the specified SEM mesh with topography, Q, and radial anisotropy, a hybrid model combining US.2016 for V_{sv} and CRUST1.0 for V_{sh} in the crust and global model S40RTS in the mantle is a good candidate for the initial model used in further FWI work.

ACKNOWLEDGEMENTS

Models GyPSuM, SEMum-NA14, US-SL-2014, US.2016, S362ANI and AK135 are downloaded from the website of the Incorporated Research Institutions for Seismology (IRIS) Earth Model Collaboration (EMC) (http://ds.iris.edu/ds/products/emc/). Models S40RTS and Krischer18 are provided by Ritsema *et al.*, (2011) and Krischer *et al.* (2018). Model CRUST1.0 is downloaded from the REM website (https://igppweb.ucsd.edu/gabi/crust1.html). Seismic data are downloaded from the International Federation of Digital Seismograph Networks (FDSN, https://www.fdsn.org), Canadian National Seismic Network (CNSN, http://www.earthquakescanada.nrcan.gc.ca) and Servicio Sismológico Nacional (SSN, http://www.ssn.unam.mx). [Adding network citations] Detailed networks used with dois are listed below:

CI: California Institute of Technology and United States Geological Survey Pasadena. (1926). Southern California Seismic Network [Data set]. International Federation of Digital Seismograph Networks. https://doi.org/10.7914/SN/CI

CN: Natural Resources Canada (NRCAN Canada). (1975). Canadian National Seismograph Network [Data set]. International Federation of Digital Seismograph Networks. https://doi.org/10.7914/SN/CN

II: Scripps Institution of Oceanography. (1986). Global Seismograph Network - IRIS/IDA [Data set]. International Federation of Digital Seismograph Networks. https://doi.org/10.7914/SN/II

IU: Albuquerque Seismological Laboratory (ASL)/USGS. (1988). Global Seismograph Network - IRIS/USGS [Data set]. International Federation of Digital Seismograph Networks. https://doi.org/10.7914/SN/IU

MX: Servicio Sismológico Nacional. (2017). https://doi.org/10.21766/SSNMX/SN/MX

TA: IRIS Transportable Array. (2003). USArray Transportable Array [Data set]. International Federation of Digital Seismograph Networks. https://doi.org/10.7914/SN/TA.

US: Albuquerque Seismological Laboratory (ASL)/USGS. (1990). United States National Seismic Network [Data set]. International Federation of Digital Seismograph Networks. https://doi.org/10.7914/SN/US

UW: University of Washington. (1963). Pacific Northwest Seismic Network - University of Washington [Data set]. International Federation of Digital Seismograph Networks. https://doi.org/10.7914/SN/UW

[end of adding network citations]

The earthquake CMT solutions are from the global CMT webpage (https://www.globalcmt.org). The open-source spectral-element software package SPECFEM3D_GLOBE and the moment-tensor inversion package CMT3D used for this paper are freely available for download via the Computational Infrastructure for Geodynamics (CIG, https://geodynamics.org). Digital data of outlines of LIPS and hotspot locations are downloaded from http://www-udc.ig.utexas.edu/external/plates/data.htm. We thank Lion Krischer, Scott Burdick and Incorporated Research Institutions for Seismology (IRIS) EMC for providing all the tomographic models. We also thank Lion Krischer, Andrew J. Schaeffer, Xyoli Pérez-Campos and Robert Herrmann for their constructive discussion and suggestion regarding seismic model implementation or data acquisition. The seismic waveform data were downloaded from IRIS Data Management Center. We thank the Institute for Cyber-Enabled Research (ICER) at Michigan State University and the Extreme Science and Engineering Discovery Environment (XSEDE supported by NSF grant ACI-1053575) for providing the high-performance computing resources. This research was supported by NSF grant 1942431 and the startup fund of Min Chen at Michigan State University.

Here, we express our great sorrow to the passing of our co-author Dr Min Chen. Min was our loved colleague, advisor, teacher and friend. Min was a brilliant seismologist and her research aimed to better understand plate tectonics and earthquake ruptures using high-resolution seismic images produced by FWI. Min worked tirelessly to improve diversity, equity and inclusion in the geoscience community. Min was always passionate about life and was always ready to help her students, colleagues and friends all over the world—from Asia, America to Africa. She indeed passed on her kind heart and smile to every friends. Min left us too soon. The world lost a growing mind in seismology, a thoughtful advisor, and a good mother (most importantly for her two daughters, Vivian and Mia). It is very hard to say goodbye to Min. With deepest condolences, we hope Min rest in peace forever.

REFERENCES

Alex Song, T.-R. & Helmberger, D.V., 2007. Validating tomographic model with broad-band waveform modelling: an example from the la ristra transect in the southwestern united states, *J. geophys. Int.,* **171**(1), 244–258.

Bao, X. & Shen, Y., 2016. Assessing waveform predictions of recent three-dimensional velocity models of the Tibetan Plateau, *J. geophys. Res.: Solid Earth,* **121,** 2521–2538.

Bedle, H. & van der Lee, S., 2009. S velocity variations beneath north america, *J. geophys. Res.: Solid Earth,* **114**(B7).

Bozdağ, E., Peter, D., Lefebvre, M., Komatitsch, D., Tromp, J., Hill, J., Podhorszki, N. & Pugmire, D., 2016. Global adjoint tomography: first-generation model, *J. geophys. Int.,* **207**(3), 1739–1766.

Bozdağ, E. & Trampert, J., 2008. On crustal corrections in surface wave tomography, *J. geophys. Int.,* **172**(3), 1066–1082.

Bozdağ, E. & Trampert, J., 2010. Assessment of tomographic mantle models using spectral element seismograms, *J. geophys. Int.,* **180**(3), 1187–1199.

Buehler, J. & Shearer, P., 2017. Uppermost mantle seismic velocity structure beneath usarray, *J. geophys. Res.: Solid Earth,* **122**(1), 436–448.

Burdick, S. *et al.*, 2017. Model update may 2016: upper-mantle heterogeneity beneath north america from travel-time tomography with global and usarray data, *Seismol. Res. Lett.,* **88**(2A), 319–325.

Chen, M., Manea, V.C., Niu, F., Wei, S.S. & Kiser, E., 2019. Genesis of intermediate-depth and deep intraslab earthquakes beneath japan constrained by seismic tomography, seismicity, and thermal modeling, *Geophys. Res. Lett.,* **46**(4), 2025–2036.

Chen, M., Niu, F., Liu, Q. & Tromp, J., 2015a. Mantle-driven uplift of hangai dome: new seismic constraints from adjoint tomography, *Geophys. Res. Lett.,* **42**(17), 6967–6974.

Chen, M., Niu, F., Liu, Q., Tromp, J. & Zheng, X., 2015b. Multiparameter adjoint tomography of the crust and upper mantle beneath east asia: 1. Model construction and comparisons, *J. geophys. Res.: Solid Earth,* **120**(3), 1762–1786.

Chen, M., Niu, F., Tromp, J., Lenardic, A., Lee, C.-T.A., Cao, W. & Ribeiro, J., 2017. Lithospheric foundering and underthrusting imaged beneath tibet, *Nat. Commun.,* **8,** 15659.

Coffin, M.F. *et al.*, 2005. Large igneous provinces, *Encycl. Geol.,* 315–323, doi.org/10.1029/93RG02508.

Coleman, J.L.Jr & Cahan, S.M., 2012. Preliminary catalog of the sedimentary basins of the United States: U.S. Geological Survey Open-File Report 2012–1111, 27 p. (plus 4 figures and 1 table available as separate files), http://pubs.usgs.gov/of/2012/1111/.

Ekström, G., Nettles, M. & Dziewoński, A., 2012. The global cmt project 2004–2010: centroid-moment tensors for 13,017 earthquakes, *Phys. Earth planet. Inter.,* **200,** 1–9.

Engdahl, E.R., van der Hilst, R. & Buland, R., 1998. Global teleseismic earthquake relocation with improved travel times and procedures for depth determination, *Bull. seism. Soc. Am.,* **88**(3), 722–743.

Ferreira, A., Woodhouse, J., Visser, K. & Trampert, J., 2010. On the robustness of global radially anisotropic surface wave tomography, *J. geophys. Res.: Solid Earth,* **115**(B4).

Fichtner, A., Kennett, B.L., Igel, H. & Bunge, H.-P., 2009. Full seismic waveform tomography for upper-mantle structure in the australasian region using adjoint methods, *J. geophys. Int.,* **179**(3), 1703–1725.

Fichtner, A., Kennett, B.L., Igel, H. & Bunge, H.-P., 2010. Full waveform tomography for radially anisotropic structure: new insights into present and past states of the australasian upper mantle, *Earth planet. Sci. Lett.,* **290**(3–4), 270–280.

Gao, H. & Shen, Y., 2012. Validation of shear-wave velocity models of the pacific northwest, *Bull. seism. Soc. Am.,* **102**(6), 2611–2621.

Gao, H. & Shen, Y., 2015. Validation of recent shear wave velocity models in the united states with full-wave simulation, *J. geophys. Res.: Solid Earth,* **120**(1), 344–358.

Jia, Z., Ni, S., Chu, R. & Zhan, Z., 2017. Joint inversion for earthquake depths using local waveforms and amplitude spectra of rayleigh waves, *Pure appl. Geophys.,* **174**(1), 261–277.

Jiang, C., Schmandt, B., Hansen, S.M., Dougherty, S.L., Clayton, R.W., Farrell, J. & Lin, F.-C., 2018. Rayleigh and s wave tomography constraints on subduction termination and lithospheric foundering in central california, *Earth planet. Sci. Lett.,* **488,** 14–26.

Kennett, B.L., Engdahl, E. & Buland, R., 1995. Constraints on seismic velocities in the earth from traveltimes, *J. geophys. Int.,* **122**(1), 108–124.

Komatitsch, D. *et al.*, 9999. SPECFEM3D GLOBE v7.0.0 [software], Computational Infrastructure for Geodynamics, https://geodynamics.org/cig/software/specfem3d_globe/.

Komatitsch, D. & Tromp, J., 2002a. Spectral-element simulations of global seismic wave propagation—I. Validation, *J. geophys. Int.,* **149**(2), 390–412.

Komatitsch, D. & Tromp, J., 2002b. Spectral-element simulations of global seismic wave propagation—II. Three-dimensional models, oceans, rotation and self-gravitation, *J. geophys. Int.,* **150**(1), 303–318.

Krischer, L., Fichtner, A., Boehm, C. & Igel, H., 2018. Automated large-scale full seismic waveform inversion for north america and the north atlantic, *J. geophys. Res.: Solid Earth,* **123**(7), 5902–5928.

Kustowski, B., Ekström, G. & Dziewoński, A., 2008. Anisotropic shear-wave velocity structure of the earth's mantle: a global model, *J. geophys. Res.: Solid Earth,* **113**(B6).

Laske, G., Masters, G., Ma, Z. & Pasyanos, M., 2013. Update on crust1. 0-a 1-degree global model of earth's crust, in *Geophys. Res. Abstr.,* vol. **15,** p. 2658, EGU General Assembly Vienna, Austria.

Lee, E.-J., Chen, P. & Jordan, T.H., 2014. Testing waveform predictions of 3D velocity models against two recent Los Angeles earthquakes, *Seismol. Res. Lett.,* **85**(6), 1275–1284.

Lekić, V. & Romanowicz, B., 2011. Inferring upper-mantle structure by full waveform tomography with the spectral element method, *J. geophys. Int.,* **185**(2), 799–831.

Lin, F.-C., Schmandt, B. & Tsai, V.C., 2012. Joint inversion of rayleigh wave phase velocity and ellipticity using usarray: constraining velocity and density structure in the upper crust, *Geophys. Res. Lett.,* **39**(12).

Lin, F.-C., Tsai, V.C. & Schmandt, B., 2014. 3-d crustal structure of the western united states: application of Rayleigh-wave ellipticity extracted from noise cross-correlations, *J. geophys. Int.,* **198**(2), 656–670.

Lin, Y.-P., Zhao, L. & Hung, S.-H., 2011. Assessment of tomography models of Taiwan using first-arrival times from the TAIGER active-source experiment, *Bull. seism. Soc. Am.,* **101**(2), 866–880.

Liu, Q., Polet, J., Komatitsch, D. & Tromp, J., 2004. Spectral-element moment tensor inversions for earthquakes in Southern California, *Bull. seism. Soc. Am.,* **94**(5), 1748–1761.

Liu, Y., Teng, J., Xu, T., Wang, Y., Liu, Q. & Badal, J., 2016. Robust time-domain full waveform inversion with normalized zero-lag cross-correlation objective function, *J. geophys. Int.,* **209**(1), 106–122.

Maceira, M., Larmat, C., Porritt, R.W., Higdon, D.M., Rowe, C.A. & Allen, R.M., 2015. On the validation of seismic imaging methods: finite frequency or ray theory?, *Geophys. Res. Lett.,* **42,** 323–330.

Maggi, A., Tape, C., Chen, M., Chao, D. & Tromp, J., 2009. An automated time-window selection algorithm for seismic tomography, *J. geophys. Int.,* **178**(1), 257–281.

Montelli, R., Nolet, G., Masters, G., Dahlen, F. & Hung, S.-H., 2004. Global p and pp traveltime tomography: rays versus waves, *J. geophys. Int.,* **158**(2), 637–654.

Mulder, W. & Plessix, R.-E., 2008. Exploring some issues in acoustic full waveform inversion, *Geophys. Prospect.,* **56**(6), 827–841.

Nelson, P.L. & Grand, S.P., 2018. Lower-mantle plume beneath the yellowstone hotspot revealed by core waves, *Nat. Geosci.,* **11**(4), 280–284.

Panning, M., Lekić, V. & Romanowicz, B., 2010. Importance of crustal corrections in the development of a new global model of radial anisotropy, *J. geophys. Res.: Solid Earth,* **115**(B12).

Pavlis, G.L., Sigloch, K., Burdick, S., Fouch, M.J. & Vernon, F.L., 2012. Unraveling the geometry of the farallon plate: synthesis of three-dimensional imaging results from usarray, *Tectonophysics,* **532,** 82–102.

Porritt, R.W., Allen, R.M. & Pollitz, F.F., 2014. Seismic imaging east of the rocky mountains with usarray, *Earth planet. Sci. Lett.,* **402,** 16–25.

Qin, Y., Capdeville, Y., Montagner, J.-P., Boschi, L. & Becker, T.W., 2009. Reliability of mantle tomography models assessed by spectral element simulation, *J. geophys. Int.,* **177**(1), 125–144.

Ritsema, J., Deuss, A., Van Heijst, H. & Woodhouse, J., 2011. S40rts: a degree-40 shear-velocity model for the mantle from new rayleigh wave dispersion, teleseismic traveltime and normal-mode splitting function measurements, *J. geophys. Int.,* **184**(3), 1223–1236, doi.org/10.1111/j.1365-246X.2010.04884.x.

Ritsema, J., Van Heijst, H., Woodhouse, J. & Deuss, A., 2009. Long-period body wave traveltimes through the crust: implication for crustal corrections and seismic tomography, *J. geophys. Int.,* **179**(2), 1255–1261.

Robertsson, J.O., 1996. A numerical free-surface condition for elastic/viscoelastic finite-difference modeling in the presence of topography, *Geophysics,* **61**(6), 1921–1934.

Ruan, Y., Lei, W., Modrak, R., Örsvuran, R., Bozdağ, E. & Tromp, J., 2019. Balancing unevenly distributed data in seismic tomography: a global adjoint tomography example, *J. geophys. Int.,* **219**(2), 1225–1236.

Schmandt, B. & Humphreys, E., 2010. Complex subduction and small-scale convection revealed by body-wave tomography of the western united states upper mantle, *Earth planet. Sci. Lett.,* **297**(3–4), 435–445.

Schmandt, B. & Lin, F.-C., 2014. P and s wave tomography of the mantle beneath the united states, *Geophys. Res. Lett.,* **41**(18), 6342–6349.

Schmandt, B., Lin, F.-C. & Karlstrom, K.E., 2015. Distinct crustal isostasy trends east and west of the rocky mountain front, *Geophys. Res. Lett.,* **42**(23), 10–290.

Shen, W. & Ritzwoller, M.H., 2016. Crustal and uppermost mantle structure beneath the united states, *J. geophys. Res.: Solid Earth,* **121**(6), 4306–4342.

Simmons, N.A., Forte, A.M., Boschi, L. & Grand, S.P., 2010. Gypsum: a joint tomographic model of mantle density and seismic wave speeds, *J. geophys. Res.: Solid Earth,* **115**(B12).

Taborda, R., Azizzadeh-Roodpish, S., Khoshnevis, N. & Cheng, K., 2016. Evaluation of the southern California seismic velocity models through simulation of recorded events, *J. geophys. Int.,* **205,** 1342–1364.

Tao, K., Grand, S.P. & Niu, F., 2017. Full-waveform inversion of triplicated data using a normalized-correlation-coefficient-based misfit function, *J. geophys. Int.,* **210**(3), 1517–1524.

Tao, K., Grand, S.P. & Niu, F., 2018. Seismic structure of the upper mantle beneath eastern asia from full waveform seismic tomography, *Geochem. Geophys. Geosyst.,* **19**(8), 2732–2763.

Tape, C., Liu, Q., Maggi, A. & Tromp, J., 2010. Seismic tomography of the southern california crust based on spectral-element and adjoint methods, *J. geophys. Int.,* **180**(1), 433–462.

Tromp, J., Tape, C. & Liu, Q., 2005. Seismic tomography, adjoint methods, time reversal and banana-doughnut kernels, *J. geophys. Int.,* **160**(1), 195–216.

van der Kruk, J. *et al.*, 2015. Quantitative multi-layer electromagnetic induction inversion and full-waveform inversion of crosshole ground penetrating radar data, *J. Earth Sci.,* **26**(6), 844–850.

Yuan, H., French, S., Cupillard, P. & Romanowicz, B., 2014. Lithospheric expression of geological units in central and eastern north america from full waveform tomography, *Earth planet. Sci. Lett.,* **402,** 176–186.

Zhou, T., Meng, L., Xie, Y. & Han, J., 2019. An adjoint-state full-waveform tsunami source inversion method and its application to the 2014 chile-iquique tsunami event, *J. geophys. Res.: Solid Earth,* **124**(7), 6737–6750.

Zhu, H., Bozdağ, E., Duffy, T.S. & Tromp, J., 2013. Seismic attenuation beneath Europe and the North Atlantic: implications for water in the mantle, *Earth planet. Sci. Lett.,* **381,** 1–11.

Zhu, H., Komatitsch, D. & Tromp, J., 2017. Radial anisotropy of the north american upper mantle based on adjoint tomography with usarray, *J. geophys. Int.,* **211**(1), 349–377.

SUPPORTING INFORMATION

Supplementary data are available at *GJI* online.

Figure S1 Example of earthquake source parameters re-inversion. (a) Misfit function with event depth; (b) azimuthal bins and numbers of measurements in each azimuthal bin; (c) and (d) waveform examples of the original and re-inverted earthquake event parameters.

Figure S2 Cross-section of the averaged shear wave velocity along 40°E within 1° perpendicular to the profile of models US.2016 and CRUST1.0. Star is showing the earthquake 201305240347A and triangles are showing the projection of the stations in Fig. 3(c).

Figure S3 Waveform comparison for short-period body waves. The seismic recordings are filtered between 9–20 s and aligned by the reduce time of the *S*-wave arrival predicted by AK135. Black and red lines are the data and synthetics, respectively. Blue dashed lines mark the shear wave windows and cyan lines mark the starting point of the surface wave predicted by empirical Rayleigh and Love phase speed in Table 2.

Figure S4 Waveform comparison for short-period surface wave. The seismic recordings are filtered between 9–20 s and aligned by the empirical arrival time of Rayleigh or Love waves predicted by phase speeds in Table 2. Black and red lines are the data and synthetics, respectively. Cyan dashed lines mark the surface wave measurement window. Blue dashed line indicates the end of *S*-wave window that is 60 s after *S* arrival predicted by AK135.

Figure S5 Traveltime shift distribution histograms for body wave only measurement windows. Rows upper to lower: 9–20, 20–40 and 40–120 s; panels left to right: different models.

Figure S6 Traveltime shift distribution histograms for surface wave only measurement windows. Rows upper to lower: 9–20, 20–40 and 40–120 s; panels left to right: different models.

Figure S7 Traveltime shift distribution histograms for *SV* and *SH* waves. Black and red lines and texts are for *SV* and *SH*, respectively. Rows upper to lower: 9–20, 20–40 and 40–120 s; panels left to right: different models.

Figure S8 Traveltime shift distribution histograms for Rayleigh and Love waves. Black and red lines and texts are for Rayleigh and Love, respectively. Rows upper to lower: 9–20, 20–40 and 40–120 s; panels left to right: different models.

Figure S9 Misfit functions for body wave only. Rows upper to lower: 9–20, 20–40 and 40–120 s; columns left to right: traveltime, amplitude, waveform and zero-lag CC misfits, respectively. First three models with minimum misfits are marked with different reds. The *x*-axis marks are for different models: AK: AK135, AC: AK135+CRUST1.0, UL: US-SL-2014, GY: GyPSuM, S4: S40RTS, S3: S362ANI, US: US.2016, SE: SEMum-NA14 and KR: Krischer18. Models UL, S4, S3 and SE are implemented with CRUST1.0 on top.

Figure S10 Misfit functions for surface wave only. Rows upper to lower: 9–20, 20–40 and 40–120 s; columns left to right: traveltime, amplitude, waveform and zero-lag CC misfits, respectively. First three models with minimum misfits are marked with different reds. The x-axis marks are for different models: AK: AK135, AC: AK135+CRUST1.0, UL: US-SL-2014, GY: GyPSuM, S4: S40RTS, S3: S362ANI, US: US.2016, SE: SEMum-NA14 and KR: Krischer18. Models UL, S4, S3 and SE are implemented with CRUST1.0 on top.

Figure S11 Percentage of NZCC > 0.7 of mantle model S40RTS with crustal model Crust2.0, Crust1.0 and US.2016, and model GLADM25 and US.2016 as references. From top to bottom lines are 9–20, 20–40 and 40–120 s frequency range, respectively. From left to right column are different phases in six categories (*P–SV Z*, *P–SV R*, *SH T*, Rayleigh *Z*, Rayleigh *R* and Love *T*), respectively. First three models with maximum percentage of NZCC > 0.7 measurements are marked with different reds. The *x*-axis marks are for different models: US: US.2016, SC1: S40RTS+CRUST1.0, SC2: S40RTS+CRUST2.0, SCU: S40RTS+US.2016 and M25: GLADM25.

Figure S12 Misfit functions of mantle model S40RTS with crustal model Crust2.0, Crust1.0 and US.2016, and model GLADM25 and US.2016. From top to bottom lines are 9–20, 20–40 and 40–120 s frequency range, respectively. From left to right column are traveltime, amplitude, waveform and NZCC misfits, respectively. First three models with minimum misfits are marked with different reds. The *x*-axis marks are for different models: US: US.2016, SC1: S40RTS+CRUST1.0, SC2: S40RTS+CRUST2.0, SCU: S40RTS+US.2016 and M25: GLADM25.

Figure S13 Waveform comparison of model S40RTS plus Crust1.0 in different *Q* models. Black: with 1-D *Q* from PREM; red: with constant *Q* = 600 in the crust and PREM *Q* in mantle. Event: 200802211416A, station: IU.CCM. Epicentral distance: 17.9°. Waveforms are filtered to 20–40 s.

Figure S14 Misfit functions of model S362ANI and S40RTS plus Crust1.0 in different *Q* models. From top to bottom lines are 9–20, 20–40 and 40–120 s frequency range, respectively. From left to right column are traveltime, amplitude, waveform and NZCC misfits, respectively. First three models with minimum misfits are marked with different reds. The *x*-axis marks are for different models: S3_1DQ: S362ANI with 1-D PREM Q model, S3_3DQ: S362ANI with 3-D QRF12 model, S4_1DQ: S40RTS with 1-D PREM Q model, S4_CQ: S40RTS with 1-D PREM Q model in the mantle and constant $Q =$ 600 in the crust.

Figure S15 Averaged shear wave NZCC misfit at each station for all the testing events. Stations are colour coded by NZCC misfit value in 20–40 s. Each panel are different models.